國立臺灣大學理學院大氣科學系

碩士論文

Department of Atmospheric Sciences

College of Science

National Taiwan University

Master's Thesis

用 200 百帕位勢高度來探討南亞高壓的變化特徵

Characteristics of the South Asian High variability revealed by 200hPa geopotential height

陳柏嘉

Po-Chia Chen

指導教授：盧孟明 博士

Advisor: Mong-Ming Lu, Ph.D.

中華民國 113 年 6 月

June 2024

doi:10.6342/NTU202401227

國立臺灣大學碩士學位論文
口試委員會審定書

本論文係 陳柏嘉 君（學號 R10229017 ）在國立臺灣大學大氣科學學系、所完成之碩士學位論文，於民國 113 年 1 月 17 日承下列考試委員審查通過及口試及格，特此證明

口試委員：

盧孟明 （簽名）	
（指導教授）	
曾陽治	陳中宏
羅宇婷	

系主任、所長 游政谷 （簽名）

致謝

經過兩年多的旅程，終於走到了盡頭。在這本論文的完成過程中，我要衷心感謝盧孟明老師多次耐心細心的討論指導，還有三位口試委員隋中興老師、曾開治老師和中央氣象署羅資婷科長，對論文內容所提出的問題與建議，讓我的論文更加完善。

相較於大學時期，修課不再是研究生階段的主要任務。這段期間，我擁有更多的自由時間，但總覺得自己無法有效利用這些時間。面對研究時，我常常心猿意馬，處於被動狀態，抱著得過且過的心態，甚至養成了拖延的壞習慣。這段經歷讓我深刻體會到自己在研究上的主動性不足，包括如何發現問題，以及如何靠自己解決問題的能力，這些都是我在這階段學習和成長的不足之處。儘管如此，我希望這段旅程中的點點滴滴，包括學習到的知識與分析資料的能力，都能成為我未來成長的養分。我會持續努力，讓自己成為一個具備獨立思考和解決問題能力的人。

謝謝盧孟明老師三年來耐心的指導，感謝家人的無私支持，感謝雲與氣候實驗室的夥伴們，包括賴姿伶博士、卓盈旻博士、崇瑋、爾東、威仁、靜軒、元懷、祥任、冠筠、維華、建泓、世裴、芸霆、聖丰和佩芳等夥伴，以及所有在研究上曾經幫助過我的老師和同學。謝謝你們和我討論研究、協助我解決問題，並陪伴我度過碩士生涯。還要感謝那些因為我瘋狂愛上看演唱會，而幫我搶票，讓我能參加很多演唱會的朋友們。

最後，祝福未來一切順利。

doi:10.6342/NTU202401227

中文摘要

南亞高壓 (SAH) 是亞洲夏季在上對流層最重要的反氣旋環流系統。本研究旨在分析南亞高壓的變異性及其與中緯度波動的關係。我們使用 200 hPa 的位勢高度 (Z200) 作為分析南亞高壓的變數，並以 1979-2022 在 44 年的氣候平均值覆蓋了 20-35°N，40-110°E 區域範圍的 12520 gpm 等值線作為界定南亞高壓的參考值，發現該區域內，最大 Z200 易出現在伊朗高原 (45-65°E) 和青藏高原 (80-100°E) 兩個地方。

透過對南亞高壓區域 Z200 的 EOF 分析，發現了其時空的變化特徵可用三個主模態描述。第一模態的空間特徵顯示出單極結構，中心位於伊朗高原的北部。第二模態的空間特徵呈現出東西方向反相位變化的二極結構，兩個變化中心分別在伊朗高原北部和青藏高原東北部。第三模態的空間特徵在東西方向呈現三極結構，反映了西風噴流中波導效性的波列特徵。上述結果顯示南亞高壓 Z200 的主要變化位置，是位於其北部邊界亞洲西風噴流區，並受到活躍擾動向南延伸的影響。

這些模態在時間的變異性上顯示出兩個明顯的時間尺度：準雙週 (10-20 天) 和準月度 (20-40 天)。南亞高壓上的準雙週變化，主要受到與嵌入在西風噴流波導中的渦旋和波列的影響，與這些擾動的向南延伸。中緯度地區擾動主要出現在 60-90°E 之間和 90-120°E 之間兩個地方，源自 50°N 並向南延伸，分別影響伊朗高原北部和青藏高原東北部兩個南亞高壓的變化中心。而南亞高壓上的準月度變化，則受到上游烏拉山脈附近的阻塞高壓或低壓槽 (40-70°N, 30-60°E) 影響，這個地區同時也是歐亞大陸上阻塞高壓好發的地方。

最後，由 1989 年夏季個案，證實了觀察每日高度場、風場距平等氣候變數，可清楚辨識南亞高壓的準雙週變化和西風噴流波導中的渦旋，以及 60-90°E 和 90-120°E 的中緯度擾動向南延伸的影響，顯示了解南亞高壓主模態有助於詮釋

doi:10.6342/NTU202401227

中高緯度波動和亞洲季風區天氣與氣候變化的關係。

關鍵字：亞洲夏季季風、南亞高壓、準雙週振盪

doi:10.6342/NTU202401227

Abstract

The South Asian High (SAH) is the most important upper tropospheric summer system over Asia. This study aims to analyze the variability of the SAH and its relationship with the mid-latitude waves. The SAH in this study is represented by the geopotential height at 200 hPa (Z200). Its extent is defined by the 12520-gpm contour at 200 hPa, which covers the region of (20-35°N, 40-110°E) based on the 44 years of climatological mean. Within this region, the maximum Z200 tends to occur over the Iranian Plateau (45-65°E) and the Tibetan Plateau (80-100°E).

The SAH variability is further investigated by EOF analysis of the Z200 over the SAH region. The spatial pattern of the first mode displays a monopole structure with its center to the north of the Iranian Plateau. The spatial pattern of the second mode exhibits a dipole structure in east-west direction. The dipole structure comprises the primary variation center over the northeast of the Tibetan Plateau, accompanied by a secondary variation center with a reverse sign to the north of the Iranian Plateau. The variation centers of SAH variability are all located near its northern boundary where the Asian westerly jet exists. The tripole spatial structure in east-west direction of the third mode reflects geographical enhancement of the eddies trapped within the jet stream waveguide.

doi:10.6342/NTU202401227

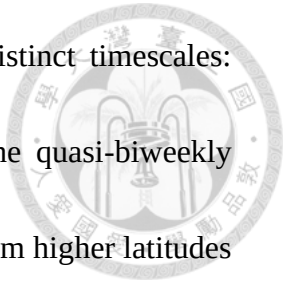

The temporal variability of the leading modes shows two distinct timescales: quasi-biweekly (10-20 days) and quasi-monthly (20-40 days). The quasi-biweekly perturbations over the SAH appear as the perturbations intruding from higher latitudes to the north of the Iranian Plateau and the northeast of the Tibetan Plateau. The quasi-monthly perturbations are strongly influenced by blocking or trough patterns between 30-60°E, situated to the northwest of the Iranian Plateau. The wave train passing through the north of the SAH, characterized by several eddies trapped within the jet stream waveguide, can be observed on both the 10-20-day and the 20-40-day timescales.

Finally, the Z200 anomalies during the summer in 1989 is presented to demonstrate that the findings in this study can be useful in climate services for interpreting real-time anomalous features in Asia The examples of 1989 confirms that the variability of the SAH on the quasi-biweekly timescale is associated with eddies embedded in the jet stream waveguide, with some influenced by the southward penetration of mid-latitude waves originating from 50°N or further north in the longitude range of 60-90°E and 90-120°E.

Key words: Asian summer monsoon, South Asian High, Quasi-biweekly oscillations

doi:10.6342/NTU202401227

Contents

doi:10.6342/NTU202401227

doi:10.6342/NTU202401227

Figure captions

doi:10.6342/NTU202401227

doi:10.6342/NTU202401227

doi:10.6342/NTU202401227

doi:10.6342/NTU202401227

doi:10.6342/NTU202401227

doi:10.6342/NTU202401227

doi:10.6342/NTU202401227

1. Introduction

In boreal summer, the Asian monsoon circulation is a dominant system over South Asia and East Asia. It includes the South Asian High (SAH) in the upper troposphere, cross-equatorial flow from the Indian Ocean to the Indian Peninsula, Bay of Bengal, and Indochina Peninsula, and the Western Pacific Subtropical High (WPSH) in the lower troposphere. The SAH is the most intense and persistent upper tropospheric anticyclone system over southern Asia during boreal summer. The SAH is a thermal high formed by the surface sensible heat over the high land and monsoon regions, and its intensity, location and structure exhibit variability in multiple timescales, including subseasonal, interannual and decadal timescale. The SAH variability is highly associated with the climate and rainfall variability of Indian summer monsoon (ISM) rainfall and East Asia summer monsoon.

Climatologically, the upper-level anticyclone is initially generated over the South China Sea due to the diabatic heating generated by convection over the southern Philippines in April (Liu et al. 2013). After the Bay of Bengal (BOB) monsoon onset in May, the southerlies transport abundant moisture into the Indochinese peninsula, and then the latent heat release which is associated with precipitation causes the anticyclonic circulation gradually shifts westward to the north of the Indochina Peninsula and intensify (Liu et al. 2013). After June, the anticyclonic circulation shifts

doi:10.6342/NTU202401227

more northward, covering the region of the Tibetan Plateau, and it continues to intensify. By July and August, the SAH reaches its mature phase, with its anticyclonic circulation extending on a much broader scale than just the Tibetan Plateau, encompassing regions from Africa to the western Pacific.

Although the SAH presents an anticyclonic circulation with an oval shape in the climatological mean field, it actually comprises two major high-pressure centers, with one located over the Iranian Plateau (west center) and the other over the Tibetan Plateau (east center). The phenomenon of bimodal distribution of the SAH major center was documented in Zhang et al. (2002). They showed that the major centers of the SAH are over the Iranian Plateau (west location, 55-65°E) and the Tibetan Plateau (east location, 82.5-92.5°E). The thermodynamics diagnosis reveals that the east center over Tibetan Plateau is associated with the diabatic heating over and near the Tibetan Plateau, while the west center over the Iranian Plateau is more related to the adiabatic heating in the free atmosphere and the diabatic heating near the surface. Afterwards, many studies have examined the bimodal characteristics of the SAH, including the east-west shift of the SAH centers and their connection, and the associated influences on the precipitation over Indian and East Asia monsoon regions (Wei et al. 2015; Yang and Li 2016; Wei et al. 2019b; Zhang et al. 2002). Wei et al. (2015) found that the SAH has a southeast–northwest (SE–NW) shift on the interannual time scale. They showed that the

doi:10.6342/NTU202401227

movement of the SAH towards the southeast (northwest) is closely linked to decreasing (increasing) ISM precipitation and increasing (decreasing) rainfall in the Yangtze River valley (YRV). They found that the latent heat released from the rainfall anomalies over the YRV can result in the SE-NW shift of the SAH. Wei et al. (2019b) confirmed that that the center locations of the SAH center are frequently over the Iranian Plateau (45-65°E) and the Tibetan Plateau (82.5-102.5°E). They found that 10–20-day is one of the dominant periods on intraseasonal time scales of the zonal shift of SAH center, and the eastward shift of SAH lags a decreasing rainfall over northern India by about 1 day, but leads an increasing rainfall over the YRV by about 3 days. Yang and Li (2016) also identified two primary center locations for the SAH, centered over the Iranian Plateau (50-62.5°E) and the Tibetan Plateau (87.5-102.5°E). They observed that the zonal shift of the SAH between two centers exhibits a dominant periodicity of 10–50 days, and found the eastward (westward) shift of the SAH corresponded to the positive (negative) rainfall anomalies in northwestern China and the negative (positive) anomalies in southern China. It indicates that the latent heat release from rainfall anomalies is associated with the variability of the SAH.

In addition to the influence of diabatic heating and latent heat release from rainfall anomalies, the variability of mid-latitude waves and Asian jet stream are another influential factor contributing to the variability of the SAH. Yang and Li (2016)

doi:10.6342/NTU202401227

demonstrated that the intraseasonal variability of the upper-tropospheric height anomaly over the eastern and western centers of the SAH, and their zonal shift are associated with the southward propagation of mid-latitude perturbations. The results of vorticity budget diagnosis suggests that the southward propagation of perturbations is primarily influenced by the advection of mean vorticity through the perturbation flow. Furthermore, a mid-latitude circumglobal teleconnection pattern called the Silk Road pattern (Enomoto, 2004) for the sector over Eurasian continent is another source of the SAH variability. Ding and Wang (2005), demonstrated that the presence of the circumglobal teleconnection during the boreal summer, is a manifestation of the waveguide effect of the jet stream. The circumglobal teleconnection, containing several positive and negative eddies through the jet stream, located to the north of the SAH. Two possible sources of the circumglobal teleconnection were proposed in their study. One is the tropical diabatic heating over the ISM region can generate an anticyclonic center in west-central Asia, and subsequently, excite a Rossby wave train extending downstream to North Pacific and North America. The other possible source is the mid-latitude Rossby wave excites near the jet exit region of the North Atlantic. It can subsequently generate an anticyclone in west-central Asia, thereby influencing the intensity of the ISM.

doi:10.6342/NTU202401227

In the present study, the first objective is to reveal the spatial and temporal patterns of the SAH subseasonal variability using geopotential height at 200hPa. Subsequently, we aim to investigate the relationship between the variability and mid-latitude large-scale waves. Finally, we will use the 1989 summer to demonstrate that the statistical findings can emerge in the SAH anomalies during a specific year. The remainder of this paper is organized as follows. The datasets and methodology are introduced in section 2. The climatological mean field of SAH and its bimodal characteristics are introduced in section 3. The spatial and temporal variational patterns of the SAH and its relationship with large-scale waves are discussed in section 4. Summary and discussion are presented in section 5.

doi:10.6342/NTU202401227

2. Data and Method

2.1 Data

In this studies, the daily reanalysis data obtained from the fifth version of European Center for Medium-Range Weather Forecasts (ECMWF) Reanalysis (ERA5) during summers (June, July, August and September) from 1979 to 2022 with 0.25°×0.25° horizontal resolution are used. The variables include geopotential height (Z), zonal wind (U) and meridional wind (V) at 200 hPa and 850hPa. The data used to represent the SAH is the geopotential height at 200 hPa (Z200). The anomalies are deviations from the climatological means from 1979 to 2020. For the precipitation data, we use the Climate Prediction Center Morphing product (CMORPH) from 1998 to 2022. For the outgoing longwave radiation (OLR), we use the data obtained from the National Oceanic and Atmospheric Administration (NOAA) during the period of from 1979 to 2022.

2.2 Method

The method of empirical orthogonal function (EOF) analysis is used to capture the dominant modes of the SAH variability. The data used for the EOF analysis is daily geopotential height anomaly at 200hPa (Z200) during 1979-2020 in June, July and August (total 42×92=3864 days) over 40-110°E, 20-35°N. The principal components (PCs) in EOF are normalized by one standard deviation of the overall time series.

doi:10.6342/NTU202401227

To investigate the dominant periods of the SAH variability, we utilized the wavelet spectrum analysis (Torrence and Compo 1998) and Lanczos filtering (Duchon, 1979). The spectrum analysis and frequency filtering are applied to the time series of the SAH index, PCs derived from the EOF analysis and the reanalysis data used in this study.

doi:10.6342/NTU202401227

3. Basic features of the SAH

3.1 Climatological field of the SAH

In this section, we will introduce the climatological field of the SAH during summer months of June, July and August. The climatological mean field (1979-2020) of geopotential height and wind at 200hPa from June to August is shown in Fig. 3-1. The 12520-gpm contour at 200 hPa (represented by the green solid line) is used as a reference to delineate the extent of the SAH (Ren et al. 2015). The figure shows a large anticyclonic circulation over Asia, characterized by a ridge along the 20-35°N latitude belt, extending from the Arabian Peninsula, Indian Peninsula, and southern Tibetan Plateau to South China. The topography map around the SAH is depicted in Fig. 3-2, it shows that the height of the Iranian Plateau is about 1,000-2,000 meters, while the Tibetan Plateau is over 3,000 meters. The large anticyclonic circulation covers a significant portion of the high terrain over the south of Iranian Plateau and Tibetan Plateau.

The seasonal evolution of the SAH represented by the climatological mean fields of the geopotential height and streamline at 200hPa in every 10 days from June and August is presented in Fig. 3-3. In early June (6/1-6/10, Fig. 3-3a), the SAH is in its developmental phase, with its center situated at the northwestern Indochina Peninsula around 20°N, 90°E. The SAH expands rapidly during mid to late June (6/11-6/30, Fig.

doi:10.6342/NTU202401227

3-3b-c), its center slightly shifts northward, and the 12520-gpm expands westward to cover the Iranian Plateau and Arabian Peninsula. In late June, the 12520-gpm contour at 200 hPa covers a large region in West Asia and East Asia, with the maximum center of Z200 located over the Himalayas and south Tibetan Plateau. In July and early August, the SAH reaches its mature phase (7/1-8/10, Fig. 3-3d-g). Fig. 3-3d shows that in addition to the primary center over the south Tibetan Plateau, another center in the west emerges over Iranian Plateau around 25-30°N, 50-60°E. The western SAH rapidly weakens during mid to late August (8/11-8/30, Fig. 3-3h-i), while the anticyclonic circulation and the location of the maximum Z200 of the eastern SAH vividly remains. In short, the SAH develops in June and reaches to its mature phase in July and early August. and it starts to weaken, then starts to weaken by late August.

To better understand the progression of seasonal evolution of the SAH and its interannual variations, the strength of SAH represented by area-averaged Z200 over the main circulation of the SAH (25-35°N, 20-120°E) is shown in Fig. 3-4 for June-September from 1979-2022. As discussed above, the SAH is in its developing stage in June, and reaches to its peak strength in July and August. From the latter half of August through September, the SAH gradually weakens. The interannual fluctuations and long-term intensification of the SAH are evident in Fig. 3-4. Before the year of 2008 the SAH is particularly strong in certain years such as 1988, and 1998. After 2008, strong

doi:10.6342/NTU202401227

SAH appears almost every year except 2011 and 2015. The persistently strong SAH since 2009 is a unique feature during the period of 44 years.

3.2 Bimodal distribution of the 200hPa geopotential height daily maximum

In the previous section, we pointed out that there are two centers of the SAH in early July: one over the Tibetan Plateau and the other over the Iranian Plateau. This finding aligns with previous studies (Zhang et al. 2002) that suggested the presence of two high Z200 centers within the expansive anticyclones. To identify the centers, we first determined the location of the maximum Z200 within the area of 10-40°N, 20-120°E on the daily basis, then count the frequencies of the occurrence of a maximum value along the longitude. The result of longitudinal distribution of the daily maximum values during the summer season and in each month of June-August is presented in Fig. 3-5. The bimodal pattern is evident in Fig. 3-5 in both seasonal (JJA) and monthly diagrams. The two locations with frequent maximum Z200 are the west peak near the Iranian Plateau (45-65°E), and the east peak is near the Tibetan Plateau (80-100°E). The frequency of the east peak is slightly higher than that of the west peak, but in July the frequencies over the west and east are almost equal. The locations of the peaks coincide with the topographic peaks along the latitude belt of 25-30°N in Fig. 3-2.

To further illustrate the changes of bimodal distribution of the SAH center on the decadal timescale, as what we see in Fig. 3-4, the JJA longitudinal distribution is

doi:10.6342/NTU202401227

separated into four segments: 1979-1990 (Fig. 3-6a), 1991-2000 (Fig. 3-6b), 2001-2010 (Fig. 3-6c), and 2011-2020 (Fig. 3-6d). In the period from 1979 to 1990, the longitudinal distribution of the frequencies shows one vague peak near 90-100°E and the distribution to the west of 90°E is quite flat. The bimodal pattern becomes distinct after 1991 with a decreasing tendency of the west mode. It indicates that the distribution of the SAH two centers has become more separable in recent years, and the frequency of the east center occurrences is on the rise.

Based on the two prominent frequency peaks observed in the daily location of the maximum Z200 within the SAH area, we defined two indexes to represent the west and east center of the SAH. The West Index is defined as the area mean Z200 over 25-35°N, 45-65°E (left black box in Fig. 3-7), and the East Index is defined as the area mean Z200 over 25-35°N, 80-100°E (right black box in Fig. 3-7). Fig. 3-7 shows the variance of Z200 within the SAH area and the surrounding regions. The variance of Z200 exhibits the maximum meridional gradient within the SAH area, and the variance of Z200 in the region of the West Index is slightly larger than that in the region of the East Index. Moreover, the temporal characteristics of two indexes revealed by their spectrum power density (Fig. 3-8) show significant signals at the 95% confidence level within the quasi-biweekly (6-20-day) timescale. The spatial and temporal variability of the

doi:10.6342/NTU202401227

SAH and the relationship with high-latitude large-scale waves, as what is reflected in the large variance in Fig. 3-7, will be discussed in the next chapter.

doi:10.6342/NTU202401227

4. Leading modes of the SAH

To understand the sub-seasonal variability of the SAH, we utilize an Empirical Orthogonal Function (EOF) analysis method to capture the dominate modes of Z200 over the SAH. Subsequently, the upper-level winds and geopotential height at 200hPa are regressed on the Principal Components (PCs) of the major modes to reveal the large-scale circulations associated with the leading modes of SAH.

To eliminate the influence of the seasonal cycle, we computed the geopotential height daily anomalies by subtracting the daily means computed from 1979-2020 from the daily data before calculating the EOFs. The percentage of explained variance and North test for the top ten EOF modes is shown in Fig. 4-1. The first, second and third modes explained 41.57%, 23.18% and 12.58% of the total variance, respectively. Only the first three leading modes will be discussed because they are the most important modes that all together explains more than 75% of the total variance.

4.1 Spatial and temporal characteristics of the leading modes

The temporal characteristics of leading modes in this subsection will be presented in terms of the three-month mean and standard deviation to focus on their interannual variations, and the power spectral density of the PCs in each year and their average to reveal the intra-seasonal variations.

4.1.1 EOF1

doi:10.6342/NTU202401227

The spatial structure of the first leading mode shows that the anomalies have the same sign in the entire region of analysis, with the center of the variations over the Iranian Plateau around 35°N, 60°E (Fig. 4-2a). The three-month mean and standard deviation of the PC1 in each year from 1979-2020 (Fig. 4-3a) shows that the positive PC1 became unprecedentedly frequent since the year of 2010. Particularly noteworthy is the period of post-2015, the negative PC1 was almost entirely absent. The wavelet spectrum of PC1 (Fig. 4-4a) shows a weak signal over the entire 10-60 days band with mild power density peak that passes the 95% confidence level significance test in the quasi-biweekly timescale.

4.1.2 EOF2

The spatial structure of the second leading mode shows an east-west dipole pattern with the primary variation center over the northeastern edge of the Tibetan Plateau at 35°N, 105°E, and another variation center over the Iranian Plateau at 35°N, 65°E (Fig. 4-2b). This indicates that the second leading mode is primarily associated with Z200 variations in the eastern SAH, with anomalies of opposite sign observed in the western SAH. The three-month mean and standard deviation of the PC2 in each year from 1979-2020 (Fig. 4-3b) shows that the negative PC2 became more frequent since the year of 2009. The positive PC2 was almost absent from 2009 to 2020 except the years of 2011 and 2015. Recall that these two years are also the years with extremely weak SAH

doi:10.6342/NTU202401227

compared with other years since 2009 (Fig. 3-4). The wavelet spectrum of PC2 (Fig. 4-4b) shows the spectrum power with the period of 5-24 days exceeds the 95% confidence level which indicates that the second leading mode is closely associated with the oscillations on the quasi-biweekly timescale.

4.1.3 EOF3

The spatial structure of the third leading mode shows a tripole pattern along the latitude of 35°N (Fig. 4-2c). The tripole pattern consists of three main centers: two positive centers located over the Black Sea (35°N, 35°E) and central China (35°N, 110°E), and a negative center situated over Central Asia (35°N, 80°E). It shows that the EOF3 is mainly associated with the variations over central SAH, associated with the anomalies of opposite sign located to its east and west. The three-month mean and standard deviation of the PC3 from 1979-2020 (Fig. 4-3c) does not show obvious interannual or long-term variation patterns. However, the wavelet spectrum of PC3 (Fig.4-4c) shows a prominent spectral power density peak at approximate 14 days with a band of periods of 5-19 days exceeds the 95% confidence level.

Because both PC2 and PC3 show significant spectrum power at the quasi-biweekly timescale, in the following we check the lead-lag correlation between PC2 and PC3, with PC2 serving as the reference while shifting the time series of PC3 from -10 days to 10 days (Fig. 4-5). The result reveals that the PC2 and PC3 has the

doi:10.6342/NTU202401227

maximum correlation of 0.23 at lag 3 days, and minimum correlation of -0.29 at lead 3 days. This suggests that PC3 lags behind PC2 by approximately 3 days, which means the high pressure and low-pressure centers of EOF2 that oscillate at the quasi-biweekly timescale exhibit westward movement as what is reflected on the EOF3 variation centers (Fig. 4-2). In Section 4.3 we will continue the discussion on the quasi-biweekly oscillation components of the second and third leading modes.

4.2 The 200-hPa large-scale wind and geopotential height association with the EOF1 – the decadal variability

The most distinct feature of EOF1 is the unprecedentedly frequent positive PC1 since 2010. To understand this feature, here we present the regressed band-pass filtered winds at 200 hPa with the periods of the 10-20-days and 20-40-days. The ratios of the filtered to the total variance of PC1 are 0.107 and 0.093 for the 10-20-day and 20-40-day, respectively.

The regressed upper-level circulations and Z200 on PC1 without filtering (Fig. 4-6a) shows positive geopotential height anomalies accompanied with an anticyclonic circulation over the western part of the SAH (20-45°N, 40-80°E), which is consistent with the EOF1 pattern (Fig. 4-2a). To the north of the anticyclone, we see negative geopotential height anomalies with a weak cyclonic circulation at 50-65°N, 40-70°E.

doi:10.6342/NTU202401227

A wave train oriented in northeast-southwest direction the latitude band of 50-70°N, spanning from 0° to 120°E.

In Fig. 4-3, we see an increasing trend in positive PC1, particularly after 2010s. In order to compare the periods before and after the 2010s, we repeat the EOF analysis but for the periods of the recent 22 years from 1999 to 2020. The results show that the spatial structures and explained variances in the first modes bear a close resemblance to the analysis results of the period from 1979 to 2020 (Fig. 4-7a), with only differences in the sign. The PC1 shows a positive phase before 2010 and a negative phase afterward, indicating a decadal shift (Fig. 4-7b). Therefore, we compared the periods before and after by dividing the 22 years into two segments: 1999-2009 and 2010-2020. Anomalies were calculated as deviations from the 22-year average. The Z200 and wind anomalies during JJA during the period of 1999-2009 (Fig. 4-8a) shows negative geopotential height anomalies across most regions of the SAH. A pronounced anomalous cyclonic circulation is evident to the northwest of the SAH, centered around 40°N, 65°E. During this period, the SAH anomalies was mild and exhibited weaker intensity, particularly over the western SAH. The Z200 and wind anomalies during the period of 2010-2020 (Fig. 4-8b) shows positive anomalies almost over the entire region except the areas over northern Atlantic and central Asia. The differences between the periods of 2010-2020 and 1999-2009 (Fig. 4-8c) show positive differences across the entire domain.

doi:10.6342/NTU202401227

Particularly, there are more pronounced positive geopotential height anomalies and anomalous anticyclonic circulation to the northwest of the SAH, located around 40-60°N, 20-60°E. This indicates an increase in the intensity of blockings over that region during the period of 2010-2020.

Next, we subtract the zonal mean of Z200 at each latitude to enhance the wave structure and to see the changes in the mid-latitude wave structure during the two periods of 1999-2009 and 2010-2020 (Fig. 4-9). Firstly, in the mid-latitudes, we observe the prominent ridges over land and troughs over the oceans. Over the Eurasian Continent, two distinct ridges appear over Europe (60°N, 40°E) and eastern Siberia (60°N, 120°E), separated by a trough with the center at 70-80°E, 40-50°N. This pattern is consistently observed across both periods. The subtropical regions, also show high Z200 over land such as Asia and America and low Z200 over the Pacific and Atlantic. Note that over the ocean areas to the south of 40°N only the western North Pacific (120-150°E) is covered by high Z200. This is also the area with active summer monsoon convective activity. The high-latitude differences between these two periods of 2010-2020 and 1999-2009 (Fig. 4-9c) show positive centers over northeast America and eastern Europe, while negative centers over the Atlantic, Northeast China and Alaska. This suggests that in the later period, the trough over northeast America was weakened, while the ridge in the eastern Europe was intensified. Within the SAH region, it shows

doi:10.6342/NTU202401227

weak negative difference. The result suggests that the frequent positive PC1 anomalies after 2010 is likely to be mainly caused by the positive anomalies in the zonal mean component that was subtracted before plotting Fig. 4-9.

The regressed winds and Z200 on the PC1 (defined from section 4.1) during the periods of 1999-2009, 2010-2020, and 1999-2020 are presented in Fig. 4-10. For the period of 1999-2020 (Fig. 4-10c), the regressed pattern reveals the positive Z200 over the western SAH (20-45°N, 40-80°E) is associated with an anticyclonic circulation and positive Z200 anomalies over the entire latitudinal belt of 10-30°N. Within this latitudinal belt the zonally averaged Z200 during 2010-2020 (Fig. 4-10b) is higher than that during 1999-2009 (Fig. 4-10a). The fact supports the aforementioned speculation that the frequent positive PC1 anomalies after 2010 is likely to be caused by the positive anomalies in the zonal mean component of Z200. To the west and northwest of the SAH, we see the positive Z200 accompanied with the anticyclonic winds over Europe and a weak negative Z200 accompanied with cyclonic winds over the Mediterranean Sea. To the north of the western SAH, we see the negative Z200 over western Russia (50-70°N, 40-80°E). The regressed maps during two periods of 1999-2009 and 2010-2020 show interesting difference. During the period 1999-2009 (Fig. 4-10a), the negative geopotential height anomalies to the north of the west center of the SAH extended further, north reaching the latitudes of 70-80°N. The positive Z200 over the

doi:10.6342/NTU202401227

northeastern Atlantic is much weaker compared with Fig. 4-10c. During the period of 2010-2020 (Fig. 4-10b), the positive geopotential height anomalies over Europe and the northeastern Atlantic Ocean became more pronounced. The associated quadrupole pattern that shows the negative Z200 over the Black Sea and western Russia and positive Z200 over the western SAH is more distinct compared with Fig. 4-10a. A wave train oriented in the northwest-southeast direction from the Black Sea to the Arctic Siberia can be identified.

To further illustrate the decadal contrast of the high-latitude influence on the SAH, we plot the monthly mean Z200 anomaly averaged over the longitudinal range of 40-80°E, covering the western SAH, from 1999 to 2010 (Fig. 4-11). The figure indicates that in the tropical and subtropical region (20-40°N), negative anomalies are predominant before 2010, while positive anomalies are predominant after 2010. The predominance of positive Z200 anomalies in the tropical and subtropical region after 2010 is consistent with the observed increasing trend in PC1. However, in the higher latitudes of 50-70°N, although strong positive anomalies are more frequent after 2010, negative anomalies also appear from year to year. In order to know the relationship between Asian monsoon and the positive trend of western SAH, we plot the decadal contrast in tropical convection in the Asia summer monsoon region represented by Outgoing Longwave Radiation (OLR) and precipitation between the time periods of

doi:10.6342/NTU202401227

2010-2020 and 1999-2009 (Fig. 4-12). The results suggest that the convection (negative OLR) is stronger over the western part of India Peninsula in the later period (Fig. 4-12a), which is consistent with the wetter condition over the Indian Peninsula (Fig. 4-12b). More active convection in the tropical region implies more heating to the south of the SAH that can lead to the intensification of the western SAH and the zonal mean Z200 over the entire latitudinal belt of 10-30°N.

4.3 The 200hPa large-scale wind and geopotential height association with the EOF2 and EOF3 – the intraseasonal variability

In Section 4.1, we observed that the main variability of the second and third leading modes of the Z200 of the SAH appears at the northern edge of the SAH. The PC2 and PC3 show significant power spectrum density at the quasi-biweekly (5-25 days) timescale. For understanding the large-scale circulation patterns associated with EOF2 and EOF3, the 200-hPa winds and geopotential height data were first filtered using the periods of 10-20 days band-pass filters then regressed on the filtered PC2 and PC3 in the same frequency bands. The ratio between the variance of the 10-20-day filtered PC2 (PC3) and the total variance of PC2 (PC3) is 0.189 (0.244).

The regressed pattern on the unfiltered PC2 (Fig. 4-13a) shows a positive Z200 anomalies and anticyclonic circulation to the north of the Iranian Plateau (30-45°N, 50-80°E), and negative Z200 anomalies and cyclonic circulation to the east of the Tibetan

doi:10.6342/NTU202401227

Plateau (30-45°N, 90-120°E). These two centers are situated slightly to the north of the SAH as the EOF2 in Fig. 4-2. In the mid-latitude, there are significant negative Z200 anomalies over 50-70°N, 40-70°E, and weak positive Z200 anomalies over 50-70°N, 90-120°E. The quadrupole structure suggests that EOF2 can be sensitive to the perturbations occurred at the central point of 40-50°N and 70-100°E. The regression map of the 10-20-day filtered data (Fig. 4-13b) shows a similar pattern to the unfiltered regression map but with clearer teleconnection pattern as the wave trains originated from northeastern Atlantic. To the north of the Iranian Plateau, we see the regressed positive Z200 anomalies located to the north of the Black Sea with a regressed negative Z200 anomalies located to its east. Along the latitudinal belt of 30-50°N, an east-west elongated wave train is observed from the eastern Atlantic through the Mediterranean, the Iranian Plateau, the Tibetan Plateau, South China, and to the far northeastern Asia and Pacific. The regression map of the 20-40 day filtered data (Fig. 4-13c) reveals an intensification of negative Z200 anomalies over 50-70°N, 40-70°E and positive Z200 anomalies over 50-70°N, 90-120°E. This suggests that EOF2 has a stronger association with higher-latitude circulations on the timescale of 20-40 day, such as Rossby waves, blocking and troughs patterns over the Ural Mountain region. In summary, the regression pattern on PC2 suggests that the EOF2 of the SAH is highly correlated with circulations at higher latitudes.

doi:10.6342/NTU202401227

As for the EOF3, all the unfiltered and filtered regression maps (Fig. 4-14) show a prominent wave train teleconnection pattern along the latitudes of 25-40°N. The three variance centers along 35°N with the longitudes at 45°E, 80°E, 110°E over the SAH and embedded in the wave train is identical to the variance centers of EOF3 (Fig. 4-2). The location of the wave train corresponds closely with the jet stream within the 30-45°N, suggesting that the eddies may reflect the waveguide trapping effect of the jet stream. The teleconnection in the east-west direction is more evident in the 20-40-day filtered results (Fig. 4-14c) compared to that obtained by the 10-20-day filtering (Fig. 4-14b). The 20-40-day filtered data shows the longest wave train that originated from North Atlantic (resembling the positive phase of North Atlantic Oscillation) and extended eastward through the Mediterranean, the Iranian Plateau, the Tibetan Plateau, South China, and to the far northeastern Asia and Pacific. In summary, EOF3 reflects fluctuations in the wave train embedded in the jet stream on both the 20-40 day and 10-20 day time scales.

4.4 The relationship between mid-latitude waves and the SAH leading modes

In this section, we will show the evolution of the quasi-biweekly (10-20 days) oscillations captured by the second and third leading modes. The temporal evolution is illustrated by the correlation maps between PC and the variables of wind and geopotential height (filtered over 10-20 days) from day -7 to day 7 are presented in Fig.

doi:10.6342/NTU202401227

4-15 and Fig. 4-16.

For EOF2, Fig. 4-15 shows both of the positive correlation center in the western region (40-80°E) and the negative correlation center in the eastern region (90-110°E) on Day 0 were evolved from the positive and negative correlation centers to their northeast at 40-50°N as it is shown in the maps of Day -4 to Day -1. On Day -5 we can clear identify a positive correlation center at 70°E, 50°N that can be tracked back to Day -7 together with a negative correlation center over eastern Europe. The positive center gradually moves to the southwest and reached 50°E, 30°N on Day 0. Similarly, the negative correlation center at 110°E, 50°N on Day -4 gradually moves southwestward and reached 100°E, 30°N on Day 1. Thus, the lead-lag correlation maps suggest that the quasi-biweekly variability of EOF2 may be resulted from the southwestward penetration of mid-latitude waves originated from 50°N or further north in the longitude range of 60-90°E and 90-120°E. The characteristics of the southwestward penetration of the correlation maps of PC2 may reflect the perturbation associated with the mid-latitude Rossby wave on the time scale of 10-20 days.

For EOF3, Fig. 4-16 shows that the primary variability of the correlation centers is all situated within the latitudinal belt of 20-40°N, corresponding to the location of the jet stream. The correlation centers exhibit a slight westward movement on the time scale of 10-20 days. The characteristics are consistent with the regression maps, which

doi:10.6342/NTU202401227

indicates that eddies may be generated by the waveguide trapping effect of the jet stream.

It is known that the subtropical jet stream is an effective wave guide (Hoskins and Ambrizzi, 1993). To comprehend the progression of the seasonal evolution of the jet stream to the north of the SAH from June to August, we plot the Hovmöller diagram of climatological zonal wind averaged between 40-110°E (Fig. 4-17). The maximum position of zonal wind at 200 hPa is between 35-40°N in June, and it shifts northward to 40-45°N in July and August. The intensity of zonal wind slightly decreases in July and August compared to June.

To confirm if the observed eddies in Fig. 4-16 are linked to the waveguide trapping effect of the jet stream, we adopt the dispersion relation for barotropic Rossby waves (Hoskins and Ambrizzi, 1993) as below,

$$\omega = \bar{U}k - \frac{\beta_* k}{K^2} \tag{1}$$

where

$$\beta_* = \beta - \frac{\partial^2 \bar{U}}{\partial y^2} \tag{2}$$

is the meridional gradient of absolutely vorticity, $\bar{U}$ is the westerly flow and $K = (k^2 + l^2)^{1/2}$ is the total wave number. For stationary Rossby waves $\omega = 0$, the total wave number is determined by the equations shown below

$$K \equiv K_s = \left(\frac{\beta_*}{\bar{U}}\right)^{\frac{1}{2}} \tag{3}$$

doi:10.6342/NTU202401227

The equation (3) is possible if the flow is westerly and β_* is positive. The stationary wavenumber equation can be written on the Mercator projection as shown below

$$K_s = \left\{\left[2\Omega - \left(\frac{1}{cos\phi}\frac{\partial}{\partial\phi}\right)^2 (\cos^2\phi\,\bar{v})\right]/\bar{v}\right\}^{\frac{1}{2}} cos\phi \qquad (4)$$

where ϕ is the latitude, $\bar{v} = \overline{U}/acos\phi$ is the relative rotation of the atmosphere.

The K_s calculated from equation (4) in Asia region is presented in Fig. 4-18. $\overline{U}$ is the climatological zonal wind during summer months of June to August over the periods of 1979-2020. We observe that in the jet stream latitude range of 30-40°N the stationary wavenumber is approximately 6-7. The eddies observed in Fig. 4-16 and Fig. 4-17, the wave length is about 60-80 degrees of longitudes, which is equivalent to zonal wavenumber is about 5-6. The zonal wavenumber in the second mode is slightly smaller than the theoretical stationary wavenumber, whereas in the third mode, it closely matches the theoretical stationary wavenumber. It indicates the eddies represented by second and third leading mode are actually affected by wave guide effect within the Asian westerly jet.

4.5 Showcase of the SAH leading modes: the summer in 1989

In this section we use the year 1989 to demonstrate the relationship between mid-latitude waves and SAH on the quasi-biweekly timescale. The PC2 and PC3 in 1989 from Section 4.1 are presented in Fig. 4-19a, and the West Index and East Index defined in Section 3.2 for the year 1989 are presented in Fig. 4-19b. The PC2 and PC3 in 1989

doi:10.6342/NTU202401227

exhibit the coherent relationship, with PC3 lagging behind PC2 by approximately 2-3 days. The quasi-biweekly oscillations (QBWOs) are clearly shown in June and July with about five cycles in two months. This observation aligns with the statistical findings shown in Fig. 4-5. The relationship between PC2 and PC3 also suggests the presence of westward-moving features on the quasi-biweekly timescale. The original West Index and East Index in 1989, shown in Fig. 4-19b, are presented as bars, while the 10-20 days filtered West Index and East Index are shown as solid lines. Both the West Index and East Index exhibit quasi-biweekly oscillations in June and July. In Section 4.4, we find that the West Index and East Index are associated with southwestward penetration of perturbations from the northeast. To illustrate this, black dashed lines in Fig. 4-19b are used to present the 10-20 days filtered Z200 to the northeast of the West Index (30-50°N, 60-90°E) and East Index (30-50°N, 90-120°E). The results show that the 10-20 days filtered Z200 to the northeast of the West Index and East Index leads the West Index and East Index by about 2-3 days. This aligns with the statistical findings presented in Section 4.4.

In this paragraph, we will present the Hovmöller diagram of Z200 anomalies and the meridional component of wind at 200hPa (V200) anomalies for the year 1989 in both the time-longitude (Fig. 4-20) and latitude-time cross sections (Fig. 4-21). Fig. 4-20 shows time–longitude cross section of Z200 and V200 anomalies averaged between

doi:10.6342/NTU202401227

30-50°N, which corresponds to the position of the westerly jet. From June to July, there are several times that wave trains between 0-140°E can be clearly observed, such as on 6/1-6/10, 6/13-6/21, and 7/1-7/5, indicating the presence of eddies within the jet stream. Additionally, the wave train structures in the east appear to lag slightly compared to those in the west. In June, there are two instances where negative Z200 anomalies in 60-90°E slightly move westward to 40-60°E, while the positive Z200 anomalies in 90-120°E remain stationary. In July, two cycles of negative and positive Z200 anomalies from 90-120°E move westward to 40-60°E, with the most pronounced positive anomaly occurring from 7/20-7/31. This confirms the findings discussed in the previous section regarding the presence of westward-moving features. Fig. 4-21 shows the latitude-time cross section of Z200 and V200 anomalies averaged between 40-60°E (western part), 60-90°E (middle part), and 90-120°E (eastern part). In all three regions, the quasi-biweekly oscillations between 30-50°N are clearly observed in June and July. In the region of 90-120°E (eastern part), the quasi-biweekly oscillations are associated with the southward movement of Z200 from 50°N and further north. This indicates that the quasi-biweekly oscillations of the SAH are not only associated with eddies within the jet stream but also perturbations originating from the northern regions of the jet stream.

In the following, we will show the daily Z200 anomalies during June and July in 1989 (Fig. 4-22~4-24) to discuss the evolution of the QBWO and its relationship with

doi:10.6342/NTU202401227

the mid-latitude waves. The QBWO with the positive PC3 peaks on 6/5 (P1), 6/17 (P2), 7/3 (P3) and 7/15 (P4) can be identified in Fig. 4-19. On the first peak on 6/5, we notice the negative Z200 anomalies over 30-50°N and 70-90°E. The negative Z200 anomalies originated from the northeast and shifted southward and westward from 6/3 to 6/9. This southward intrusion created an eddy of negative Z200 anomalies trapped in the jet stream, propagating westward. For the second peak on 6/17 and the third peak on 7/3, the evolution pattern suggests that they are excited within the jet stream waveguide. Clear evidence of a wave train along the jet stream is observable from 6/13 to 6/21 and 7/1 to 7/5, with the eddies within the jet stream displaying a slightly westward movement. As for the fourth peak at 7/15, negative Z200 anomalies were observed over 30-50°N and 60-90°E. These anomalies gradually shifted southward and westward from 7/13 to 7/17, which is similar to the evolution pattern of the first peak. Additionally, another wave train along the jet stream to the north of SAH was observable from 7/19 to 7/23.

In addition to the quasi-biweekly oscillations, we also try to investigate low-frequency mid-latitude features on a quasi-monthly timescale in 1989. Fig. 4-25 displays the latitude-time cross-section of the zonal component of wind (U200) and its anomalies in a 20-day moving average for the year 1989. It shows that the jet stream is stronger in June and the first half of July, but weaker in the second half of July. Fig.

doi:10.6342/NTU202401227

4-26 displays the wind and geopotential height anomalies at 200 hPa from June to July in 1989, divided into three periods: 6/1-6/20, 6/21-7/10 and 7/11-7/31. Fig. 4-27 shows the same field with 20-40 day filtered data. In Fig. 4-26a (6/1-6/20), a wave train with a northwest-southeast orientation is observed from the mid-latitudes, with positive anomalies over 50-70°N, 30-60°E, and 30-40°N, 90-120°E, and negative anomalies over 40-50°N, 70-90°E. This wave train can also be observed in the 20-40 day filtered field (Fig. 4-27a), indicating that it is a low-frequency wave, and it has an impact on the eastern part of the SAH. In Fig. 4-26b (6/21-7/10), a weak wave train between 0-120°E in the latitude range of 30-50°N is observed, with positive anomalies between 0-90°E in the latitude range of 50-70°N to its north. However, in the 20-40 day filtered field (Fig. 4-27b), this pattern does not exist; instead, it appears only negative anomalies to the eastern part of the SAH (30-50°N, 90-120°E). In Fig. 4-26c (7/11-7/31), a clear wave train is observed to the upstream of the SAH between 30°W-60°E in the latitude range of 40-70°N. In the 20-40 day filtered field (Fig. 4-27c), this wave train becomes an arch shape in the mid-latitudes. Furthermore, positive anomalies appear to the eastern part of the SAH (30-40°N, 80-110°E). In summary, on the quasi-monthly timescale, mid-latitude waves are less pronounced, with a more dominant presence in the first half of June, primarily influencing variability in the eastern part of the SAH.

doi:10.6342/NTU202401227

5. Summary and Discussion

5.1. Summary

In this study, the variability of the SAH during the summer months of June-August is identified by using geopotential height at 200hPa. Two preferred locations of the SAH center over Iranian Plateau (45-65°E) and Tibetan Plateau (80-100°E) are identified. The variability is further investigated by EOF analysis of the Z200 over the SAH region. Three leading modes that explains more than 76% variance indicate that the variance centers are all located near the northern boundary of the SAH. Regressed large-scale wind and geopotential height field on these modes are examined to understand how the SAH variability associated with the large-scale waves.

The spatial pattern of the first mode shows a monopole structure with its center over the north of the Iranian Plateau (50-70°E). The temporal pattern, represented by PC1, suggests an increasing trend with more positive anomalies observed after 2010. The regressed upper-level circulations and Z200 on PC1 shows that the variability of the first mode is closely linked to the mid-latitude fluctuations in the North Atlantic and Ural blocking highs. The spatial pattern of the second mode displays a dipole structure in the zonal direction, The dipole structure comprises the primary variation center over the northeast of the Tibetan Plateau, accompanied by a secondary variation center with a reverse sign to the north of the Iranian Plateau. The variability of the second mode

doi:10.6342/NTU202401227

can be classified into two distinct timescales: quasi-biweekly (10-20 days) quasi-monthly (20-40 days). The temporal variability of the second mode can be classified into two distinct timescales: quasi-biweekly (10-20 days) quasi-monthly (20-40 days). On the 10–20-day timescale, the variability of EOF2 involves the southward penetration of mid-latitude waves originating from 50°N or further north, while on the 20–40-day timescale, it is linked to the low-frequency large-scale waves, particularly the Ural blockings and its associated perturbations. The spatial pattern of the third mode exhibits a tripole structure in east-west direction, and its variability are associated with the waveguide trapping effect within the jet stream. The wave train passing through the north of the SAH, characterized by several eddies within the jet stream, can be observed on both the 10-20-day and the 20-40-day timescales.

Finally, the Z200 anomalies during the summer in 1989 is presented to demonstrate the relationship between mid-latitude waves and SAH in particular on the quasi-biweekly timescale. The QBWOs in PC2 and PC3 are clearly shown in June and July, each exhibiting four cycles. In this case, we observe a southward intrusion of negative Z200 anomalies between 70-90°E, with eddies trapped within the jet stream waveguide. Additionally, clear evidence of a wave train along the jet stream is observable. It confirms that the variability of the SAH on the quasi-biweekly timescale is associated with eddies embedded in the jet stream waveguide, with some influenced

doi:10.6342/NTU202401227

by the southward penetration of mid-latitude waves originating from 50°N or further north in the longitude range of 60-90°E and 90-120°E.

5.2. Discussion

In the analysis of SAH Z200 variability, we observe that the primary center of this variability is situated at the northern edge of the SAH. We find that a portion of this variability is notably influenced by southward movement of oscillations originating from the mid-latitudes, aligning with the findings presented in Yang and Li (2016). They further applied vorticity budget diagnosis to explain the process of southward movement of intraseasonal perturbations, and proposed a potential positive convection-circulation feedback mechanism to explain the process of southward movement of perturbations. This indicates that the southward movement of oscillations not only influences the SAH variability but also correlates with local precipitation patterns and circulations. The influence of upper-level wave trains on the East Asia climate on the intraseasonal timescale was further examined in Yang et al. (2017). They proposed the existence of two types of upper-level wave trains originating from the Eurasian Continent. One type occurs in the quasi-biweekly (12-24 day) timescale, starting from Northern Europe and propagating southeastward to the Eastern Tibetan Plateau. The other type operates in the quasi-9-day timescale, originating from Western Europe and the Mediterranean, with eastward propagation to the Eastern Tibetan Plateau within the

doi:10.6342/NTU202401227

jet stream. Both upper-level wave trains are located at the northern edge of the SAH and influence its variability. It indicates that SAH variability caused by upstream influences can be roughly divided into two factors: midlatitude waves and eddies within the jet stream. Furthermore, they also observed that significant precursory signals, including a giant Ural Mountain Ridge and a large Lake Balkhash trough in the upper-level on the quasi-biweekly (12-24 day) timescale, which further influenced the zonal variability of the SAH. This observation aligns with our findings in the second mode, where we also identify that the blocking patterns over the Ural Mountains are associated with the variability of the SAH. Therefore, strong ridges and troughs in the upstream regions can serve as precursory signals of SAH variability. However, further research is needed to understand how these ridges and troughs influence the downstream regions.

The wave-like Silk Road pattern (SRP) is one of the major teleconnection patterns observed along the summertime Asian jet. In Kosaka et al. (2009) , they find that the main source of energy for the Asian jet is primarily through baroclinic energy conversion, while barotropic energy conversion, though weaker, is a critical factor for the preferred geographical phase of the wave train. They also show that the preferred geographical phase for the wave-like SRP is indeed caused by the mean state of the Asian jet. However, there are significant differences in the mean state of the Asian jet between June and July to August, including variations in zonal position and strength.

doi:10.6342/NTU202401227

The Asian jet is situated more poleward, and its wind speed is relatively smaller during July to August compared to June. In Hong et al. (2018), they compared the SRP between early and late summer, find that the SRP is stronger and more geographically fixed in late summer. Furthermore, they also show that the SRP is closely connected with the North Atlantic Oscillation (NAO), and it can efficiently trigger the SRP to propagate along the Asian jet in late summer, but not in early summer. This indicate that the Asian jet is more influenced by circulations upstream in late summer compared to early summer. Therefore, when discussing the influence of the Asian jet on the variability of the SAH, it may be necessary to separate June from July to August due to the significant differences in the mean state.

Another important feature in our study is that the combination of the second and third modes shows a westward-moving wave train. The result is associated with the rapid westward movement of low-PV air in the SAH, a phenomenon known as “eddy shedding”. In Amemiya and Sato (2020), they demonstrated a westward-moving large-scale geopotential anomaly pattern along the subtropical jet on the quasi-biweekly timescale. They found that the movement of low-PV air is mainly controlled by passive advection, and the zonal flux at 360K is mainly westward between 30 and 120°E. The westward eddy shedding breaking off from the Tibetan anticyclone can be observed several times during a summer and is confined to the upper troposphere (Popovic and

doi:10.6342/NTU202401227

Plumb 2001). Previous studies have also aimed to investigate the factors influencing this variability. One explanation is that the variability is generated by convective forcing in southeast Asia. In Amemiya and Sato (2020), they revealed that statistically significant OLR anomalies were in phase with geopotential anomalies over the southern Tibetan Plateau and southern China. Another explanation is that the variability driven by dynamical instability of two-dimensional anticyclonic flow, and the idea has been supported by studies using nonlinear models (Hsu and Plumb 2000).

In our study, we utilize geopotential height at 200 hPa to define the SAH. However, it's important to acknowledge that there are some limitations associated with this approach. The first limitation is that in the context of global warming, a significant increase in geopotential height has been observed of the SAH (Zhang et al. 2021). Our results demonstrate an increasing trend in the time series of PC1 of the SAH, with notable variability observed both before and after 2010. This indicates the conventional definition of the SAH using geopotential height at 200 hPa may reflect the changes arise from the natural variability of the SAH and the impacts of global warming. Therefore, employing corrective methods such as the eddy geopotential height used in Zhang et al. (2021) may better describe the variability of the SAH within the context of global warming. Another limitation is that the geopotential height at 200 hPa primarily reflects influences in the mid-latitudes and does not effectively capture the impact in

doi:10.6342/NTU202401227

the tropics. This is due to the larger variance of geopotential height at 200 hPa in the mid-latitudes and its smaller variance in the tropics. The findings of this study suggest an association between variability of the SAH and upstream waves in the mid-latitudes. However, due to the smaller variance of geopotential height at 200 hPa in the tropics, we did not examine the tropical influences. The connection between the western Pacific Subtropical High (WPSH) in the lower troposphere and the SAH is another important topic. Previous studies suggested the eastward extension of SAH is accompanied with the westward extension of WPSH, and it's associated with the increasing precipitation over the Yangtze River region and decreasing precipitation over the South China (Ren et al. 2015; Wei et al. 2019a). Studies in these directions may be conducted in future research.

doi:10.6342/NTU202401227

References

Amemiya, A., and K. Sato, 2020: Characterizing quasi-biweekly variability of the Asian monsoon anticyclone using potential vorticity and large-scale geopotential height field. *Atmos Chem Phys*, **20**, 13857–13876, https://doi.org/10.5194/acp-20-13857-2020.

Ding, Q., and B. Wang, 2005: Circumglobal Teleconnection in the Northern Hemisphere Summer*. *J Clim*, **18**, 3483–3505, https://doi.org/10.1175/JCLI3473.1.

Duchon, C. E., 1979: Lanczos Filtering in One and Two Dimensions. *Journal of Applied Meteorology*, **18**, 1016–1022, https://doi.org/10.1175/1520-0450(1979)018<1016:LFIOAT>2.0.CO;2.

ENOMOTO, T., 2004: Interannual Variability of the Bonin High Associated with the Propagation of Rossby Waves along the Asian Jet. *Journal of the Meteorological Society of Japan. Ser. II*, **82**, 1019–1034, https://doi.org/10.2151/jmsj.2004.1019.

Hong, X., R. Lu, and S. Li, 2018: Differences in the Silk Road Pattern and Its Relationship to the North Atlantic Oscillation between Early and Late Summers. *J Clim*, **31**, 9283–9292, https://doi.org/10.1175/JCLI-D-18-0283.1.

Hoskins, B. J., and T. Ambrizzi, 1993: Rossby Wave Propagation on a Realistic Longitudinally Varying Flow. *J Atmos Sci*, **50**, 1661–1671, https://doi.org/10.1175/1520-0469(1993)050<1661:RWPOAR>2.0.CO;2.

Hsu, C. J., and R. A. Plumb, 2000: Nonaxisymmetric Thermally Driven Circulations and

doi:10.6342/NTU202401227

Upper-Tropospheric Monsoon Dynamics. *J Atmos Sci*, **57**, 1255–1276, https://doi.org/10.1175/1520-0469(2000)057<1255:NTDCAU>2.0.CO;2.

KOSAKA, Y., H. NAKAMURA, M. WATANABE, and M. KIMOTO, 2009: Analysis on the Dynamics of a Wave-like Teleconnection Pattern along the Summertime Asian Jet Based on a Reanalysis Dataset and Climate Model Simulations. *Journal of the Meteorological Society of Japan. Ser. II*, **87**, 561–580, https://doi.org/10.2151/jmsj.87.561.

Liu, B., G. Wu, J. Mao, and J. He, 2013: Genesis of the South Asian High and Its Impact on the Asian Summer Monsoon Onset. *J Clim*, **26**, 2976–2991, https://doi.org/10.1175/JCLI-D-12-00286.1.

Popovic, J. M., and R. A. Plumb, 2001: Eddy Shedding from the Upper-Tropospheric Asian Monsoon Anticyclone. *J Atmos Sci*, **58**, 93–104, https://doi.org/10.1175/1520-0469(2001)058<0093:ESFTUT>2.0.CO;2.

Ren, X., D. Yang, and X. Q. Yang, 2015: Characteristics and mechanisms of the subseasonal eastward extension of the South Asian high. *J Clim*, **28**, 6799–6822, https://doi.org/10.1175/JCLI-D-14-00682.1.

Torrence, C., and G. P. Compo, 1998: A Practical Guide to Wavelet Analysis. *Bull Am Meteorol Soc*, **79**, 61–78, https://doi.org/10.1175/1520-0477(1998)079<0061:APGTWA>2.0.CO;2.

doi:10.6342/NTU202401227

Wei, W., R. Zhang, M. Wen, B.-J. Kim, and J.-C. Nam, 2015: Interannual Variation of the South Asian High and Its Relation with Indian and East Asian Summer Monsoon Rainfall. *J Clim*, **28**, 2623–2634, https://doi.org/10.1175/JCLI-D-14-00454.1.

——, ——, ——, S. Yang, and W. Li, 2019a: Dynamic effect of the South Asian high on the interannual zonal extension of the western North Pacific subtropical high. *International Journal of Climatology*, **39**, 5367–5379, https://doi.org/10.1002/joc.6160.

——, ——, S. Yang, W. Li, and M. Wen, 2019b: Quasi-Biweekly Oscillation of the South Asian High and Its Role in Connecting the Indian and East Asian Summer Rainfalls. *Geophys Res Lett*, **46**, 14742–14750, https://doi.org/10.1029/2019GL086180.

Yang, J., Q. Bao, B. Wang, H. He, M. Gao, and D. Gong, 2017: Characterizing two types of transient intraseasonal oscillations in the Eastern Tibetan Plateau summer rainfall. *Clim Dyn*, **48**, 1749–1768, https://doi.org/10.1007/s00382-016-3170-z.

Yang, S., and T. Li, 2016: Zonal shift of the South Asian High on the subseasonal time-scale and its relation to the summer rainfall anomaly in China. *Quarterly Journal of the Royal Meteorological Society*, **142**, 2324–2335, https://doi.org/10.1002/qj.2826.

Zhang, D., Y. Huang, B. Zhou, and H. Wang, 2021: Is There Interdecadal Variation in the South Asian High? *J Clim*, **34**, 8089–8103, https://doi.org/10.1175/JCLI-D-21-0059.1.

ZHANG, Q., G. WU, and Y. QIAN, 2002: The Bimodality of the 100 hPa South Asia High and its Relationship to the Climate Anomaly over East Asia in Summer. *Journal of the*

doi:10.6342/NTU202401227

Meteorological Society of Japan. Ser. II, **80**, 733–744, https://doi.org/10.2151/jmsj.80.733.

doi:10.6342/NTU202401227

Figures

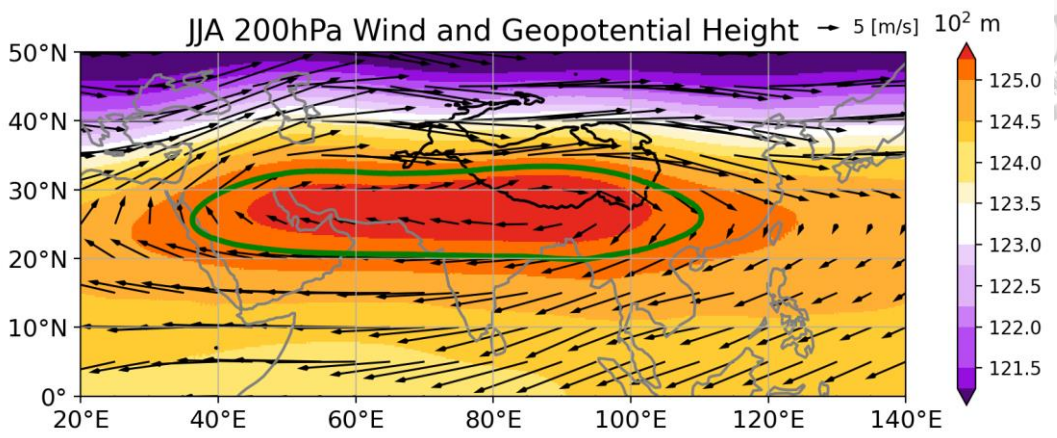

Fig. 3-1. Climatological field (1979-2020) of horizontal wind (vector, unit: m/s) and geopotential height (shading, unit: m) at 200 hPa during June, July and August. The black solid line indicates the plateau region with elevation of 3000 m and the green solid line indicates the geopotential height of 12520 m.

doi:10.6342/NTU202401227

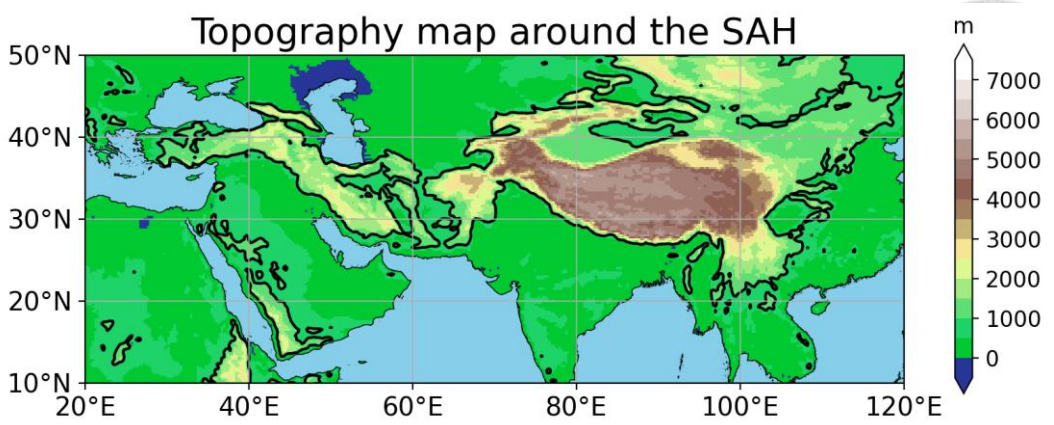

Fig. 3-2. Topography map of the Iranian Plateau, Tibetan Plateau, and the surrounding regions around the SAH. The black solid line indicates an elevation of 1000 m.

doi:10.6342/NTU202401227

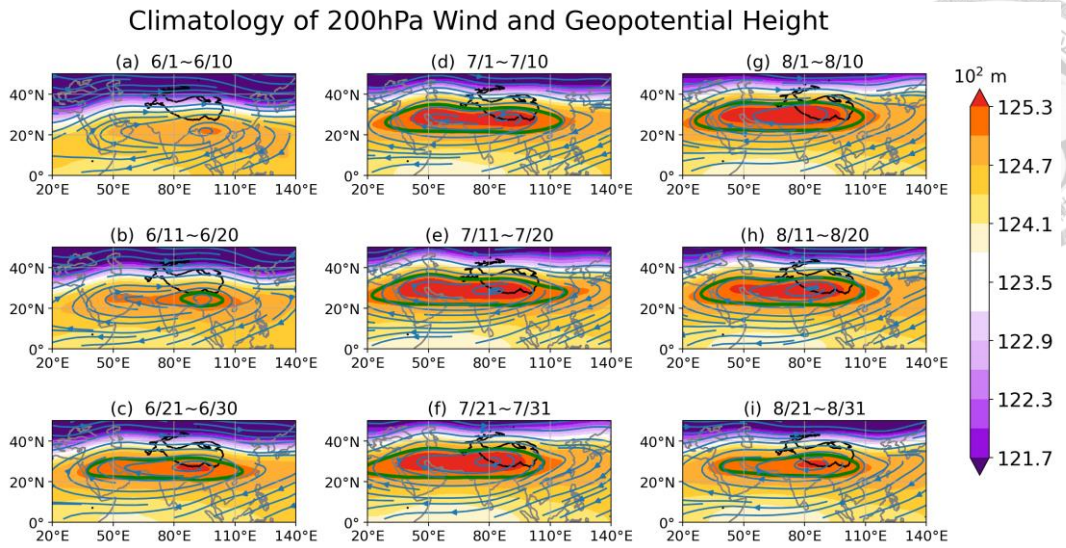

Fig. 3-3. Climatological field (1979-2020) of horizontal wind (streamline) and geopotential height (shading, unit: m) at 200 hPa in (a) 6/1~6/10 (b) 6/11~6/20 (c) 6/21~6/30 (d) 7/1~7/10 (e) 7/11~7/20 (f) 7/21~7/31 (g) 8/1~8/10 (h) 8/11~8/20 (i) 8/21~8/30. The black solid contour indicates the plateau region with elevation of 3000 m, and the green solid contour indicates the geopotential height of 12520 m.

doi:10.6342/NTU202401227

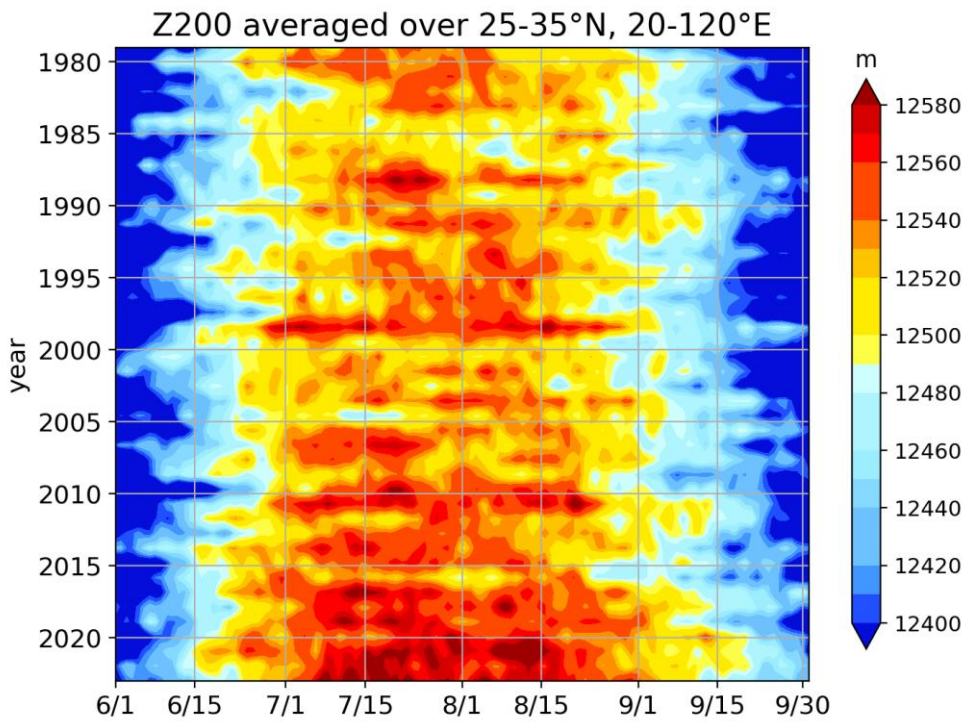

Fig. 3-4. The interannual variations of June to September seasonal evolution of the South Asian High represented by the geopotential height at 200hPa (unit: m) averaged over the region of 25-35°N and 20-120°E during the years from1979-2022.

doi:10.6342/NTU202401227

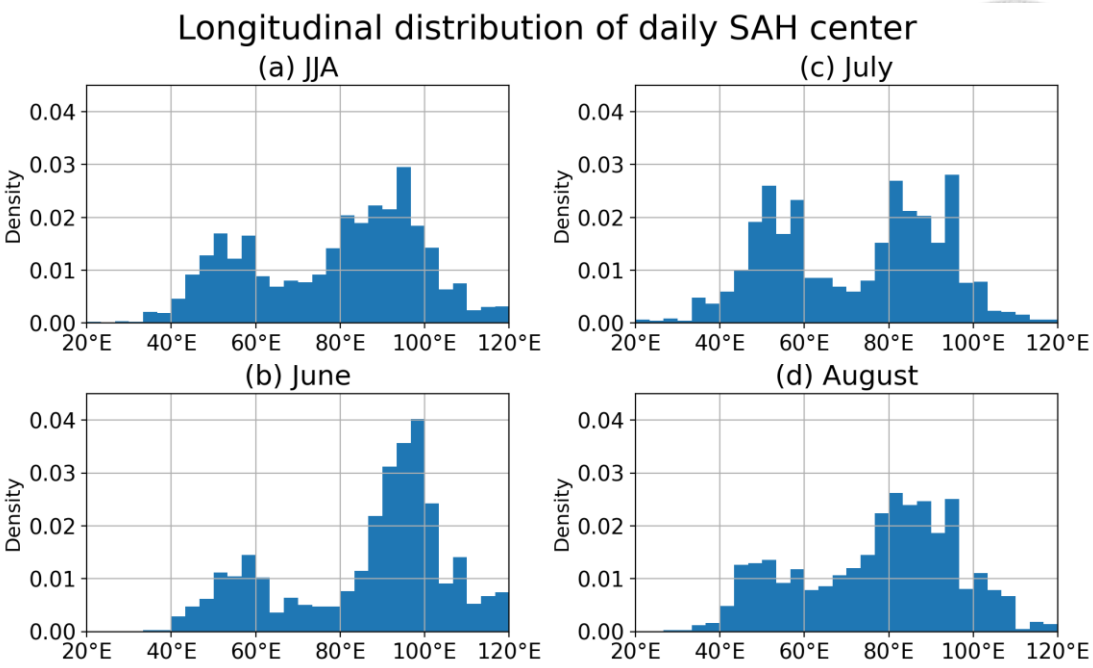

Fig. 3-5. Longitudinal distribution of the frequency of maximum value of geopotential height at 200hPa within the SAH region based on the data from 1979 to 2020 in (a) June, July and August (b) June (c) July (d) August. Each bar represents a range of 3.33 degrees of longitude.

doi:10.6342/NTU202401227

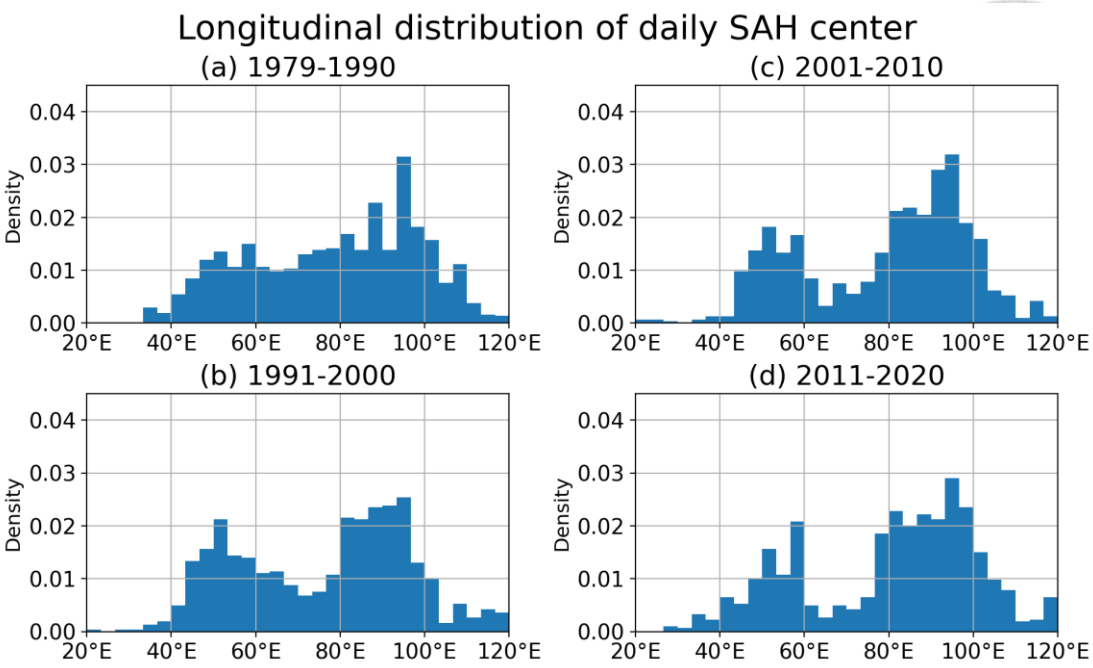

Fig. 3-6. Longitudinal distribution of the frequency of maximum value of geopotential height at 200hPa within the SAH region based on the data form (a) 1979-1990 (b) 1991-2000 (c) 2001-2010 (d) 2011-2020.in June, July and August. Each bar represents a range of 3.33 degrees of longitude.

doi:10.6342/NTU202401227

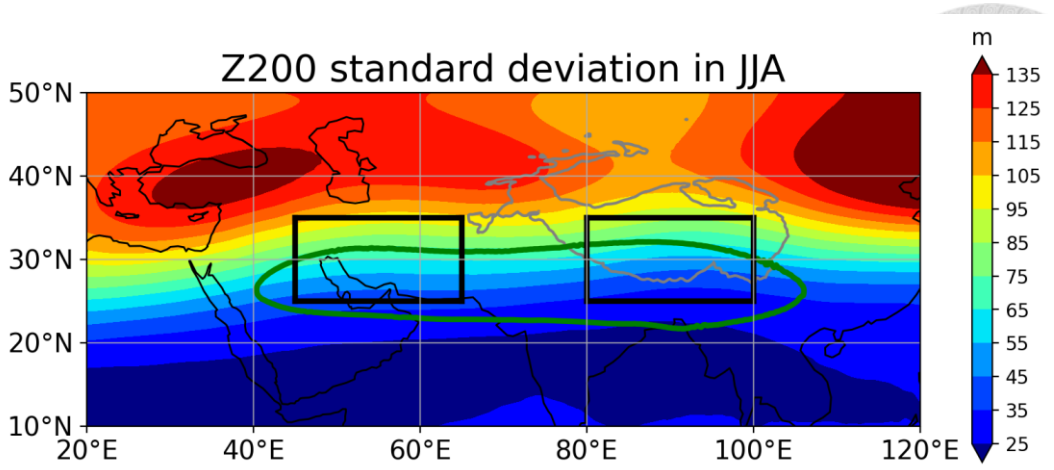

Fig. 3-7. The variance of Z200 (unit: m) within the SAH area and the surrounding regions. The two black boxes show the defined region of the West Index (25-35°N, 45-65°E) and the East Index (25-35°N, 80-100°E). The gray line represents the plateau region with an elevation of 3000 m, and the green line represents the geopotential height of 12520 m.

doi:10.6342/NTU202401227

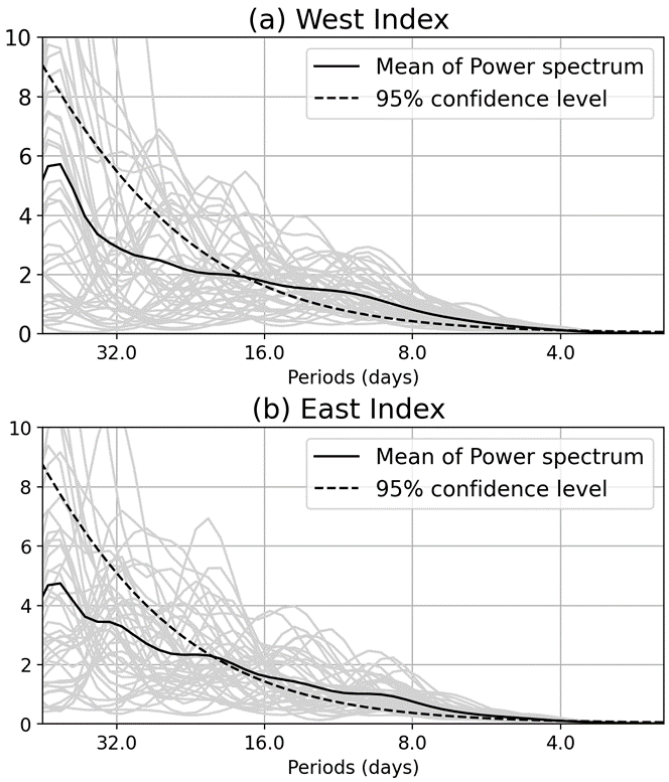

Fig. 3-8. The power spectrum of (a) the West Index (Z200 averaged over 25-35°N, 45-65°E) and (b) the East Index (Z200 averaged over 25-35°N, 80-100°E). The solid gray line represents the spectrum in each year from 1979 to 2022, and the black solid line represents the averaged value. Black dashed line represents the 95% confidence levels.

doi:10.6342/NTU202401227

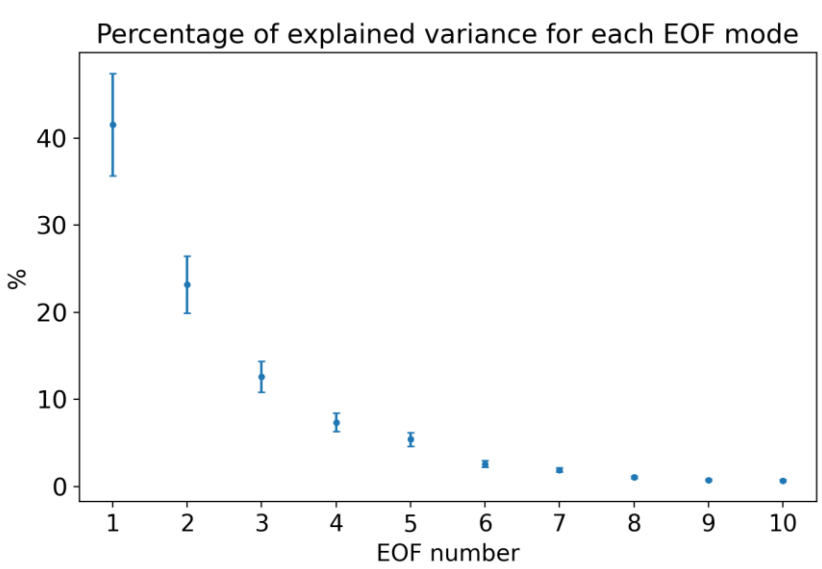

Fig. 4-1. Percentage of explained variance of the first ten EOF modes. The error bars are estimated by considering the first one hundred modes.

doi:10.6342/NTU202401227

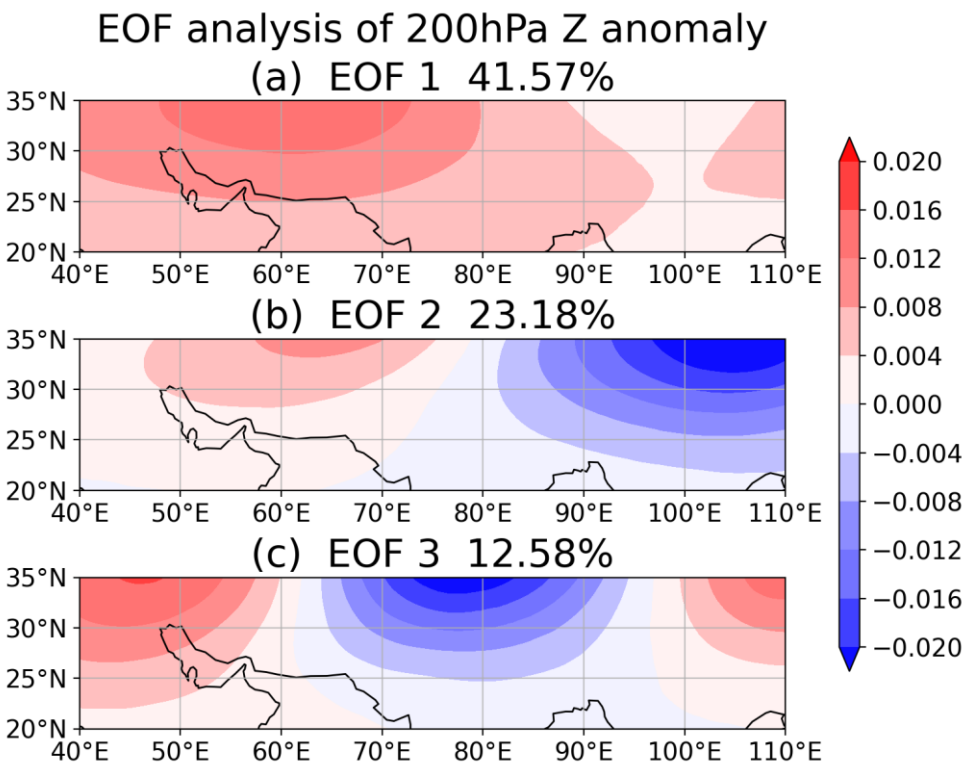

Fig. 4-2. The spatial structure of (a) EOF1, (b) EOF2 and (c) EOF3 modes in the analysis of geopotential height at 200hPa within the SAH region, based on daily data from 1979 to 2020 during June to August.

doi:10.6342/NTU202401227

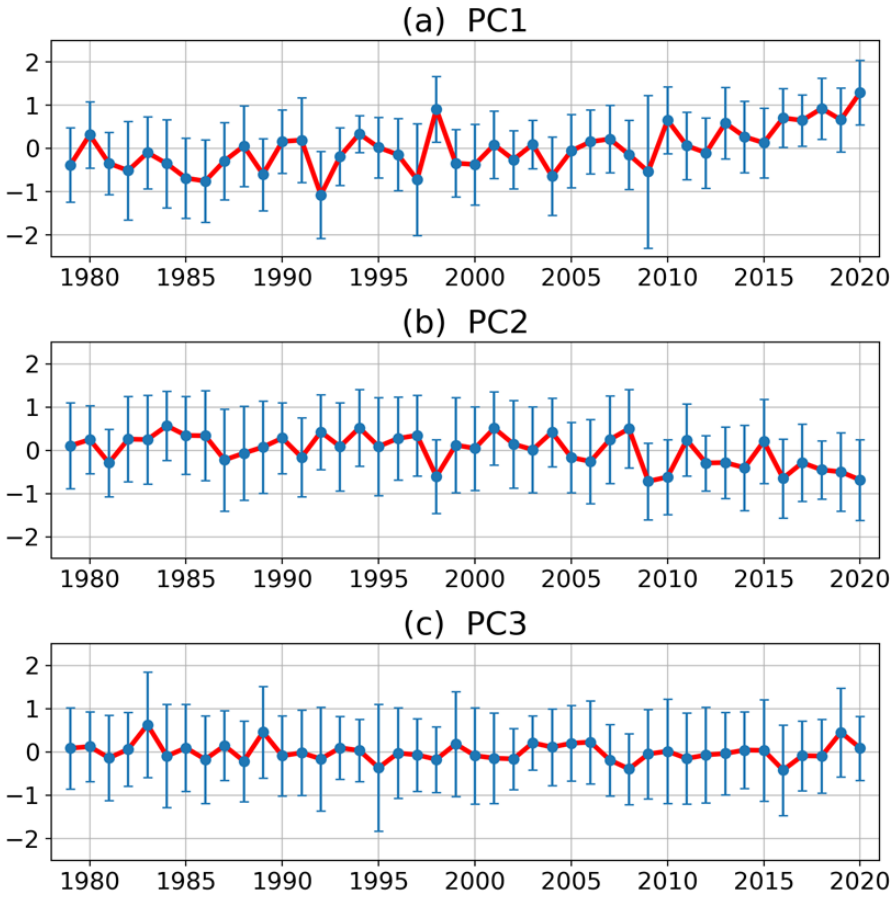

Fig. 4-3. Time series of the seasonal (JJA) mean of (a) PC1, (b) PC2 and (c) PC3 from 1979 to 2020. The error bar in each year represents the standard deviation of PC for that year.

doi:10.6342/NTU202401227

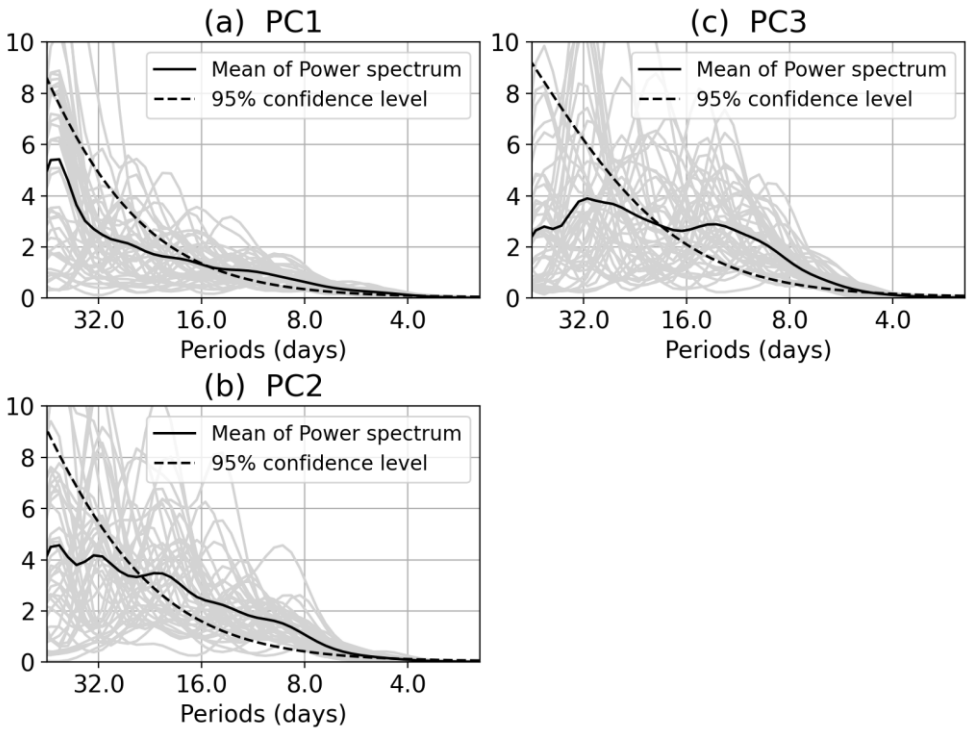

Fig. 4-4. The wavelet spectrum of (a) PC1, (b) PC2 and (c) PC3. In each figure, the gray solid lines represent the spectrum of each year from 1979 to 2020, the black solid line represents the averaged value of spectrum across all years, and the black dashed line represents the 95% confidence levels.

doi:10.6342/NTU202401227

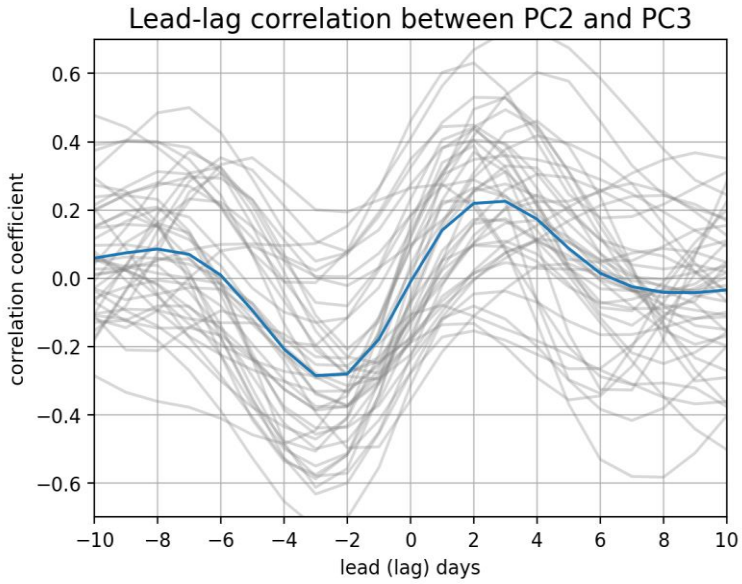

Fig. 4-5. The lead-lag correlation between PC2 and PC3. The positive lead days represents the PC3 leading, and the negative lead days represents the PC2 leading. The gray lines are the correlation in each year from 1979 to 2020, and the blue solid line represents the averaged value across all years.

doi:10.6342/NTU202401227

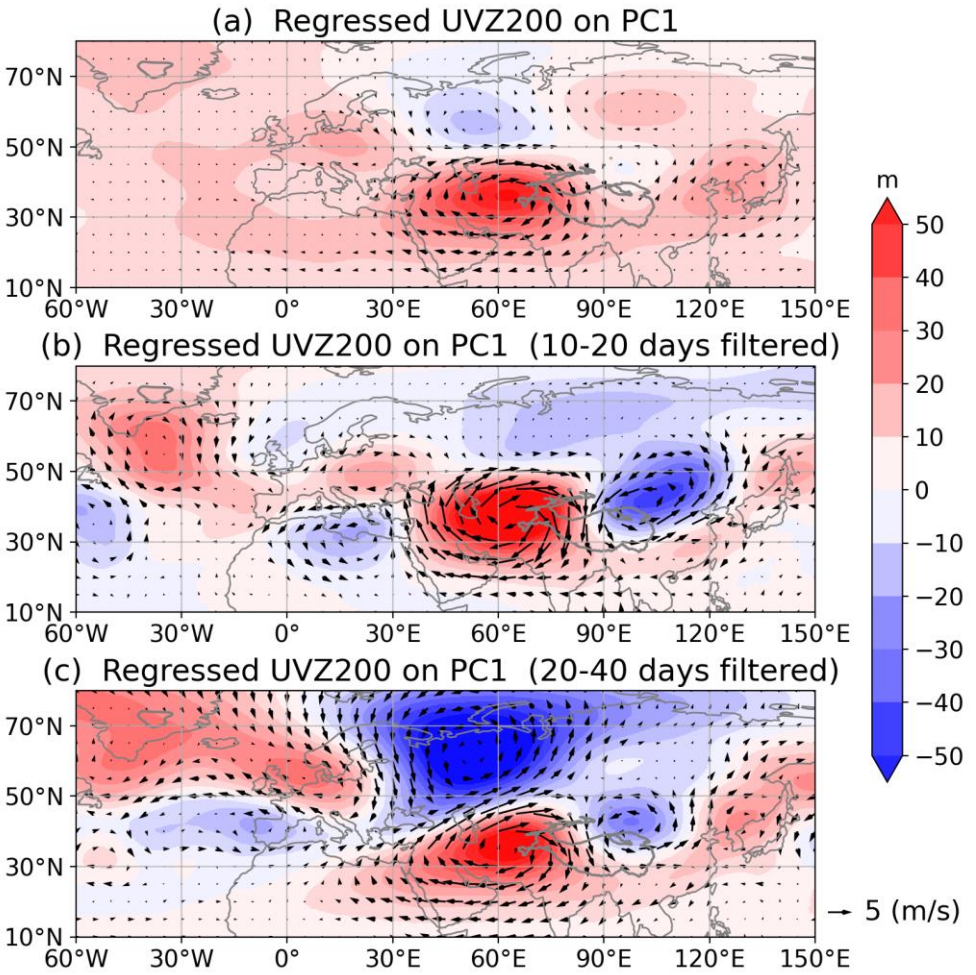

Fig. 4-6. Regressed wind (vector, unit: m/s) and geopotential height (shading, unit: m) at 200hPa on PC1, with the data are (a) unfiltered, (b) 10-20 days filtered and (c) 20-40 days filtered.

doi:10.6342/NTU202401227

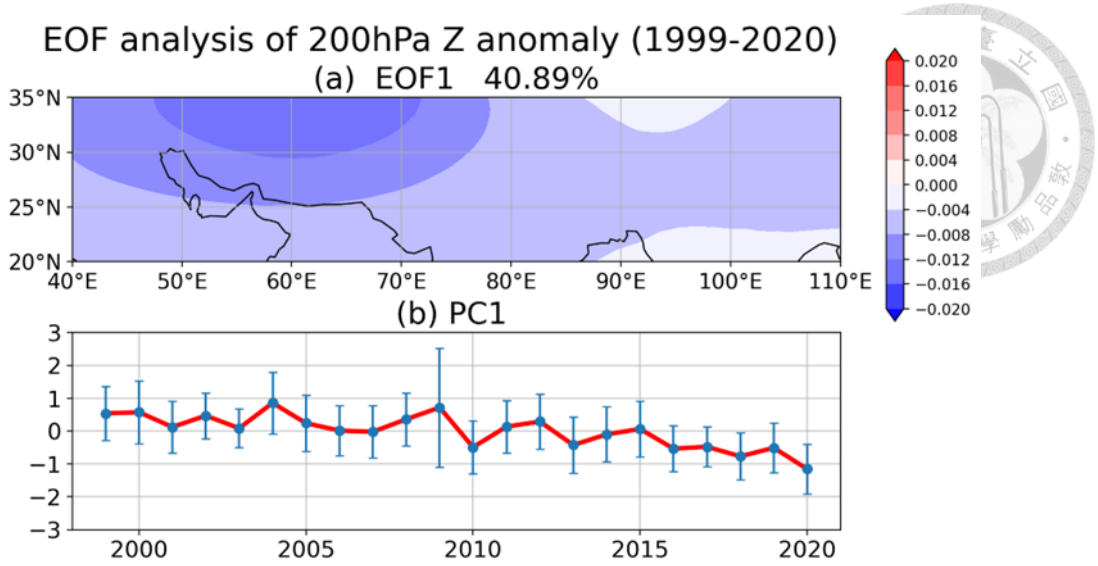

Fig. 4-7. (a) The spatial structure of EOF1 at 200hPa within the SAH region and (b) time series of the seasonal (JJA) mean of PC1 in the analysis of geopotential height, based on daily data from 1999 to 2020 during June to August.

doi:10.6342/NTU202401227

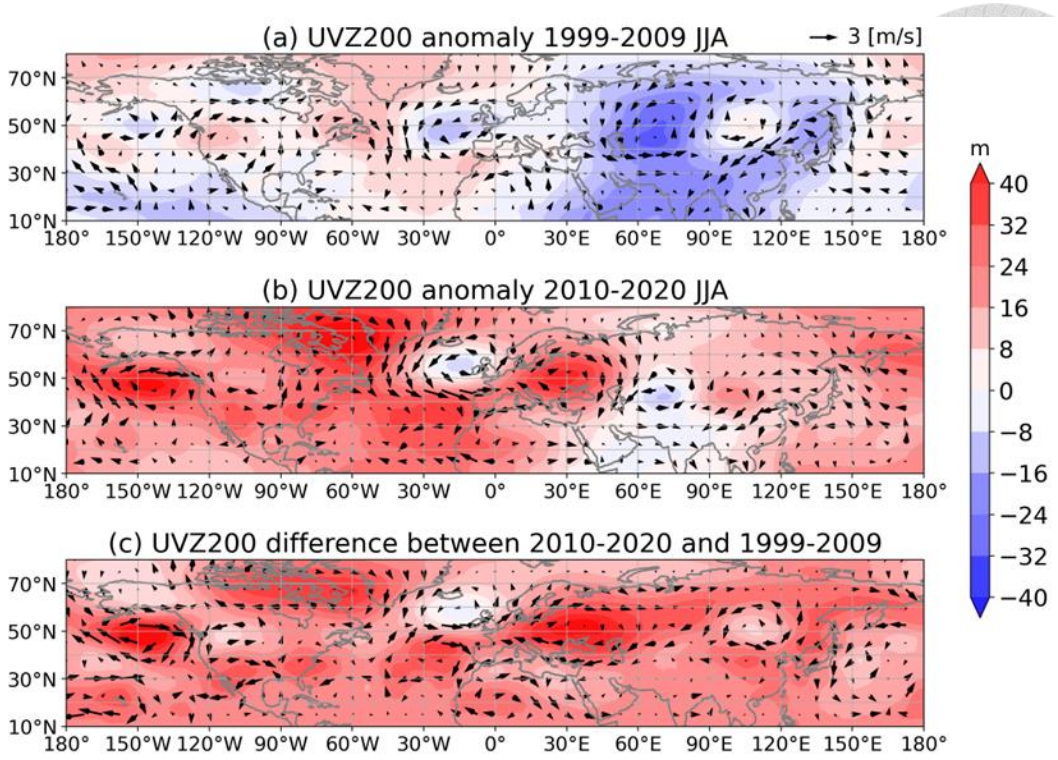

Fig. 4-8. Winds (vector, unit: m/s) and geopotential height (shading, unit: m) anomalies at 200hPa for the periods (a) 1999-2009 and (b) 2010-2020 with respect to the 42-year (1979-2020) climatology. Panel (c) represents the difference between (b) and (a).

doi:10.6342/NTU202401227

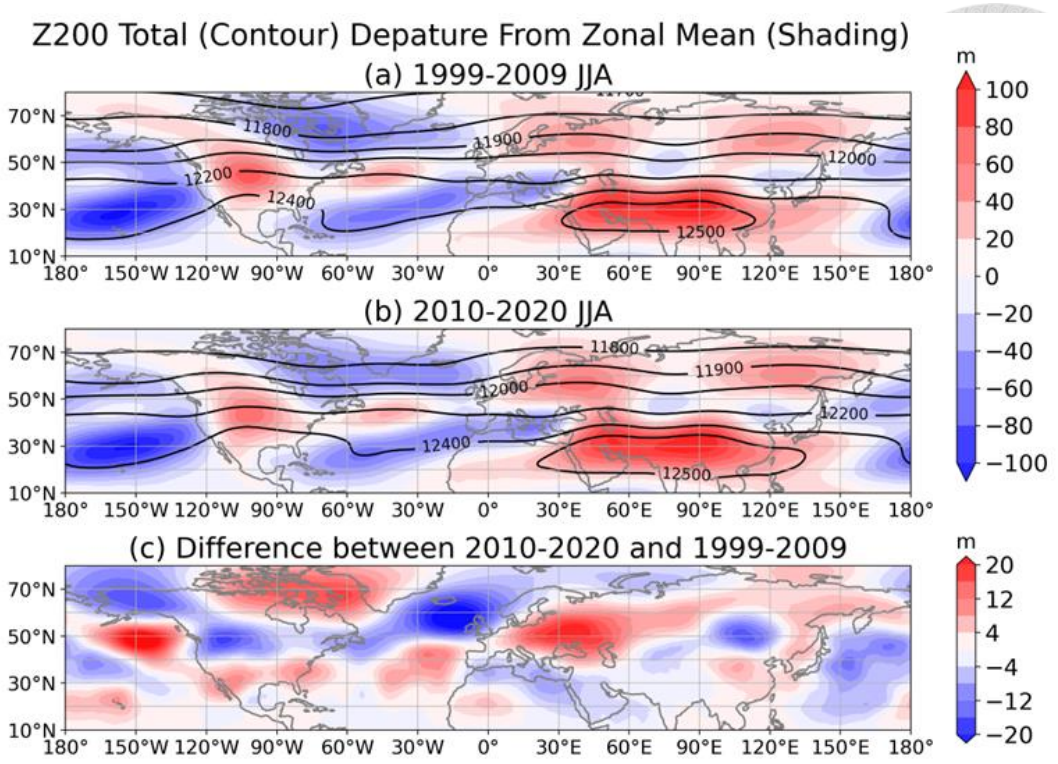

Fig. 4-9. Geopotential height at 200hPa (black contour with interval of 100 m) and its deviations from the zonal mean (shading, unit: m) over the periods (a) 1999-2009 and (b) 2010-2020. Panel (c) represents the difference between (b) and (a).

doi:10.6342/NTU202401227

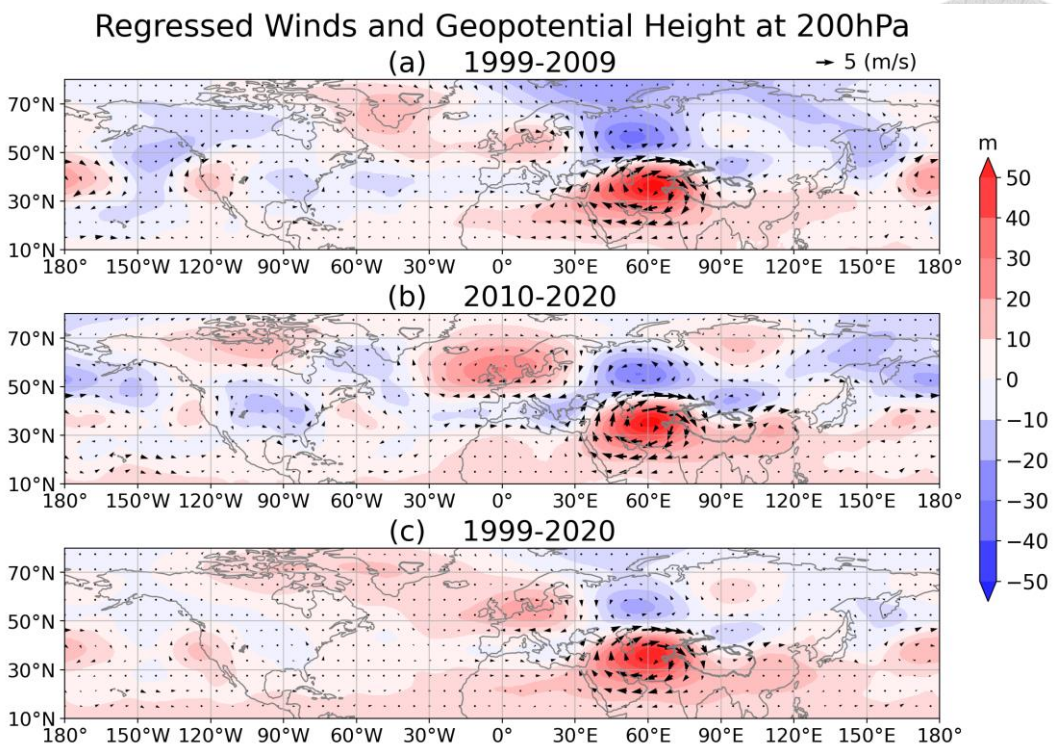

Fig. 4-10. Regressed winds (vector, unit: m/s) and geopotential height (shading, unit: m) at 200hPa on the PC1 during the periods of (a) 1999-2009, (b) 2010-2020 and (c) 1999-2020.

doi:10.6342/NTU202401227

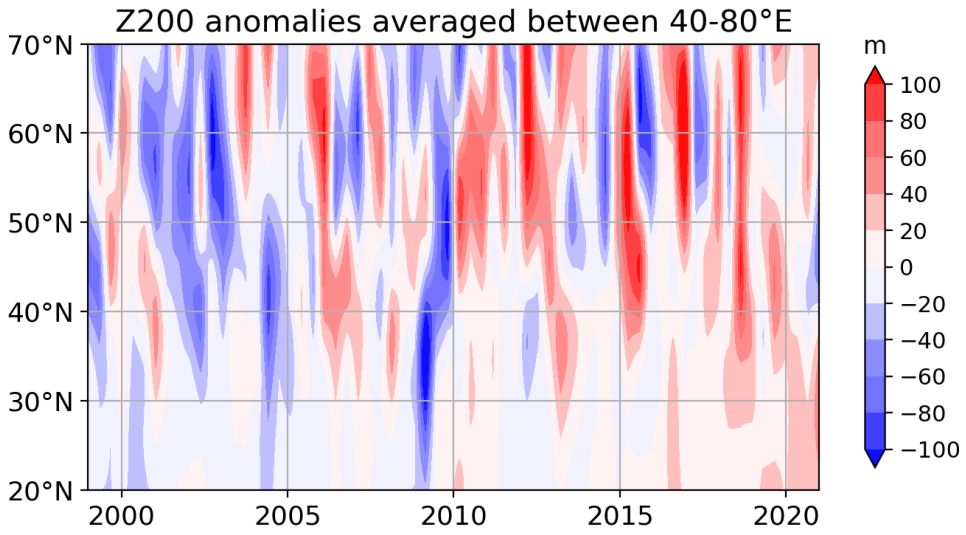

Fig. 4-11. Latitude-time cross section of monthly mean geopotential height anomalies (unit: m) at 200hPa, averaged between 40-80°E from 1999 to 2020, for the three summer months (June, July, and August) each year in the latitude range of 20-70°N.

doi:10.6342/NTU202401227

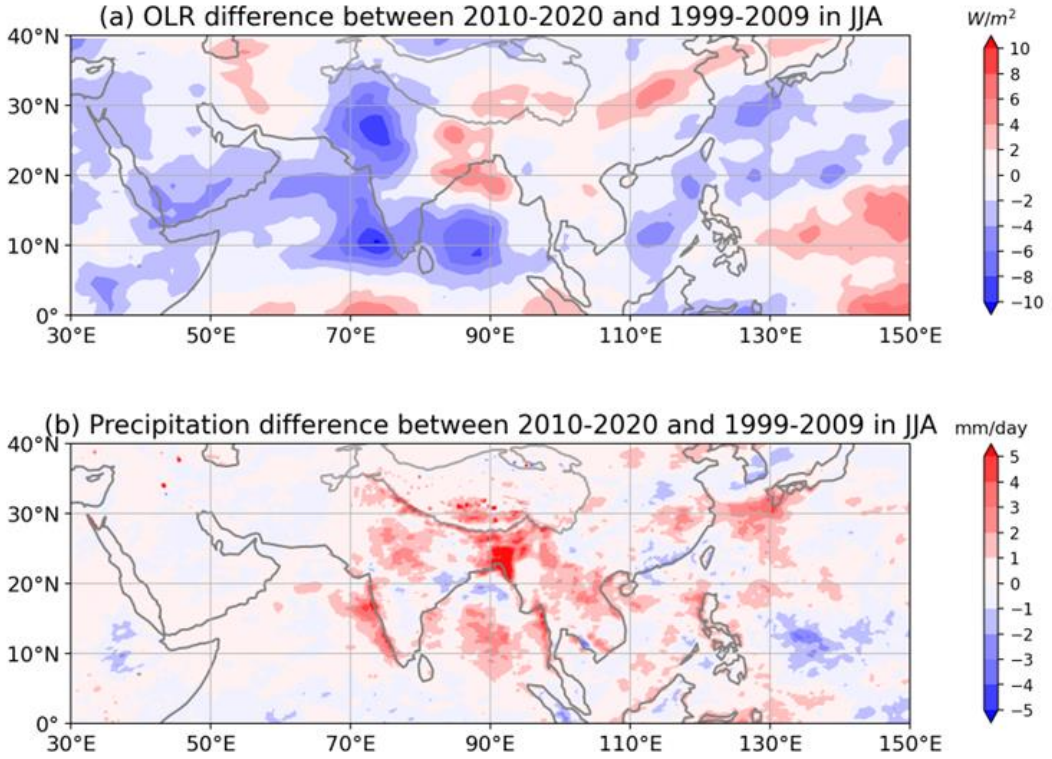

Fig. 4-12. The seasonal (June, July, August) mean of difference in (a) OLR (unit: W/m^2) and (b) precipitation (unit: mm/day) between the two periods of 2010-2020 and 1999-2009.

doi:10.6342/NTU202401227

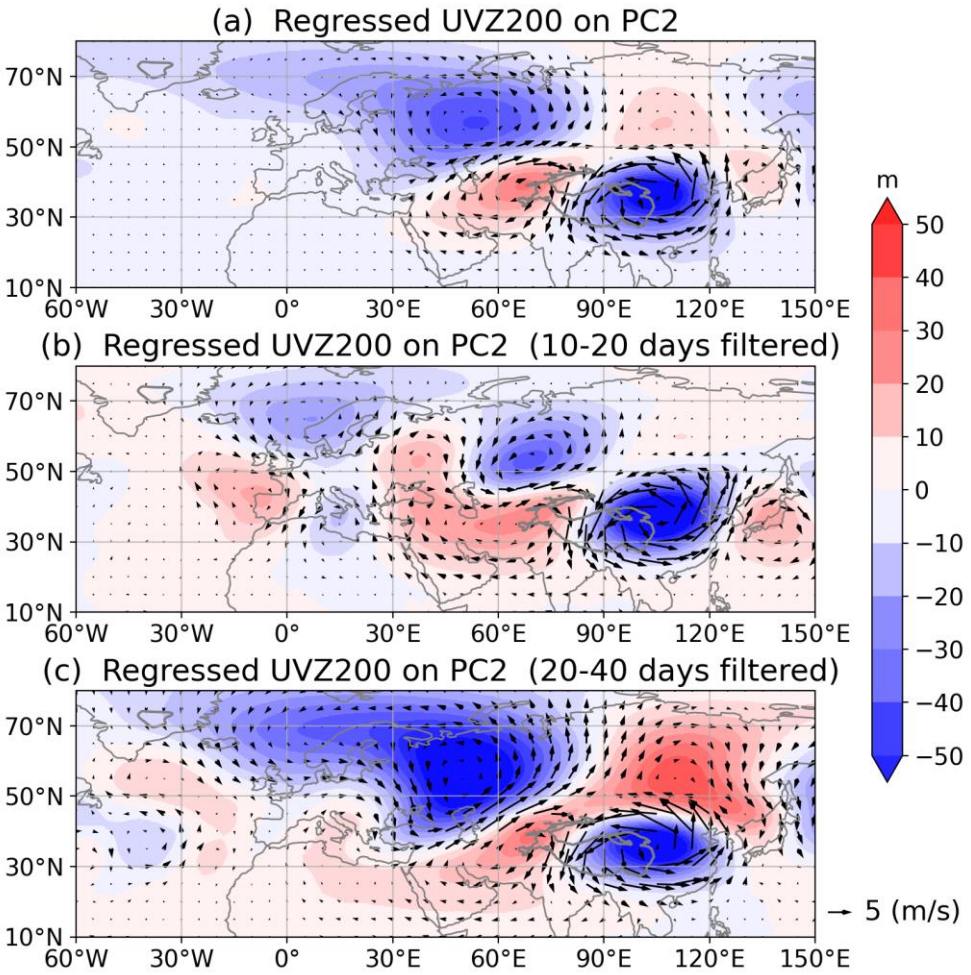

Fig. 4-13. Regressed winds (vector, unit: m/s) and geopotential height (shading, unit: m) at 200hPa on PC2, with the data are (a) unfiltered, (b) 10-20 days filtered and (c) 20-40 days filtered.

doi:10.6342/NTU202401227

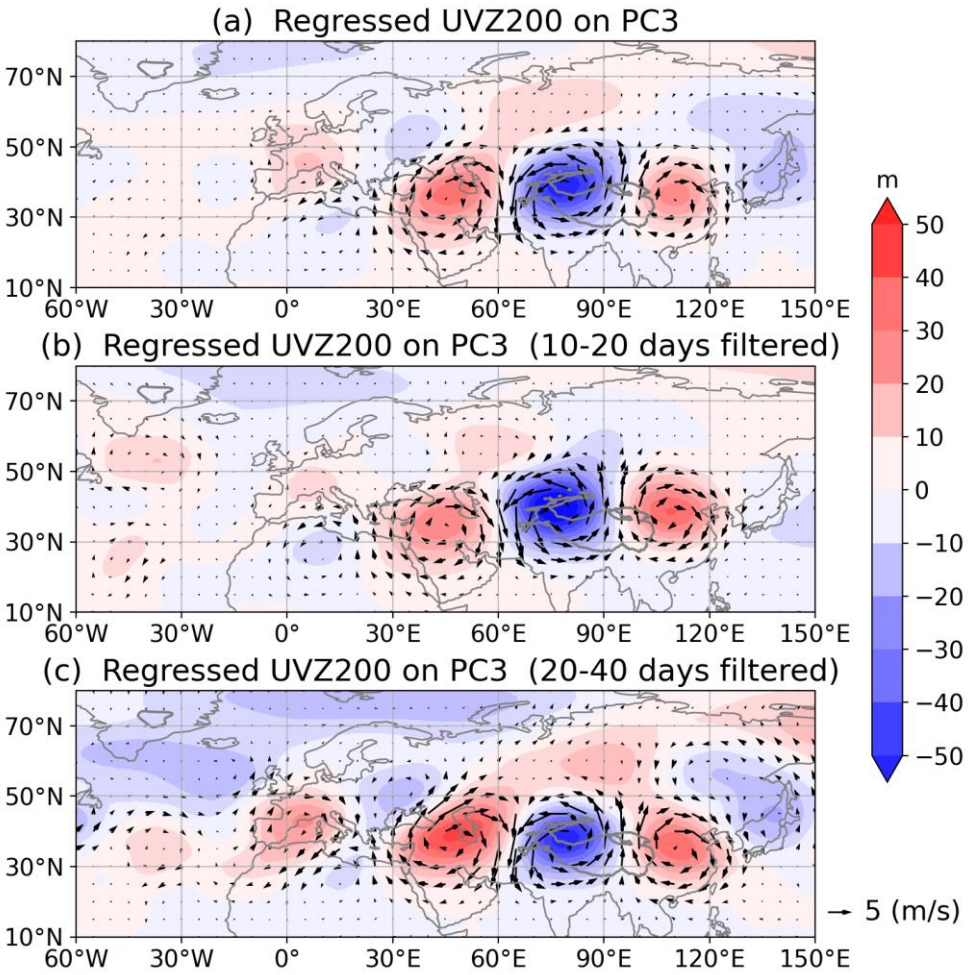

Fig. 4-14. Regressed winds (vector, unit: m/s) and geopotential height (shading, unit: m) at 200hPa on PC3, with the data are (a) unfiltered, (b) 10-20 days filtered, and (c) 20-40 days filtered.

doi:10.6342/NTU202401227

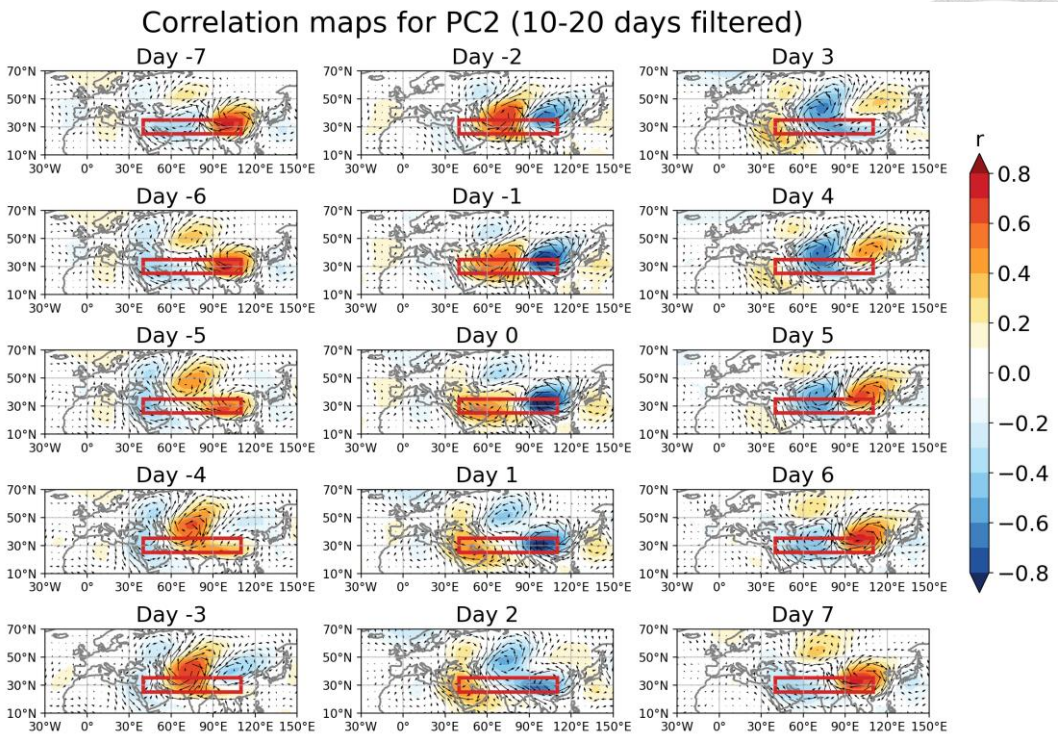

Fig. 4-15. The lead-lag correlation maps between PC2 and the variables of wind and geopotential height at 200hPa from day -7 to day 7. The data of PC2, wind and geopotential height at 200hPa are filtered over the periods of 10-20 days. The red box represents the domain of the EOF analysis (25-35°N, 40-110°E).

doi:10.6342/NTU202401227

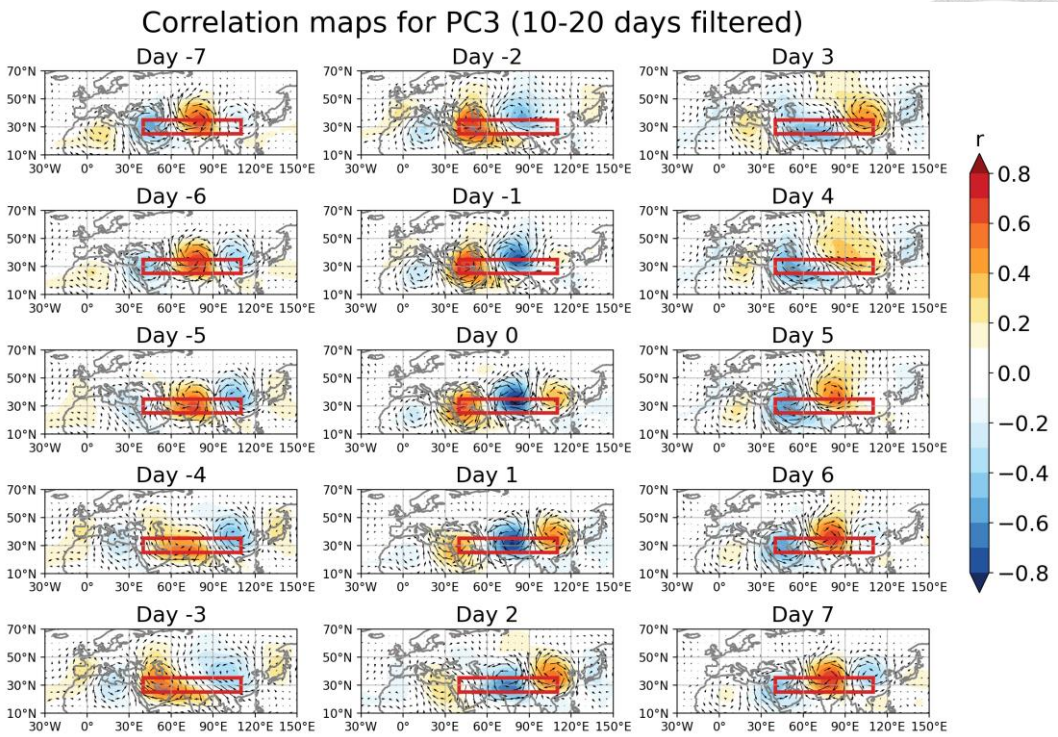

Fig. 4-16. The lead-lag correlation maps between PC3 and the variables of wind and geopotential height at 200hPa from day -7 to day 7. The data of PC3, wind and geopotential height at 200hPa are filtered over the periods of 10-20 days. The red box represents the domain of the EOF analysis (25-35°N, 40-110°E).

doi:10.6342/NTU202401227

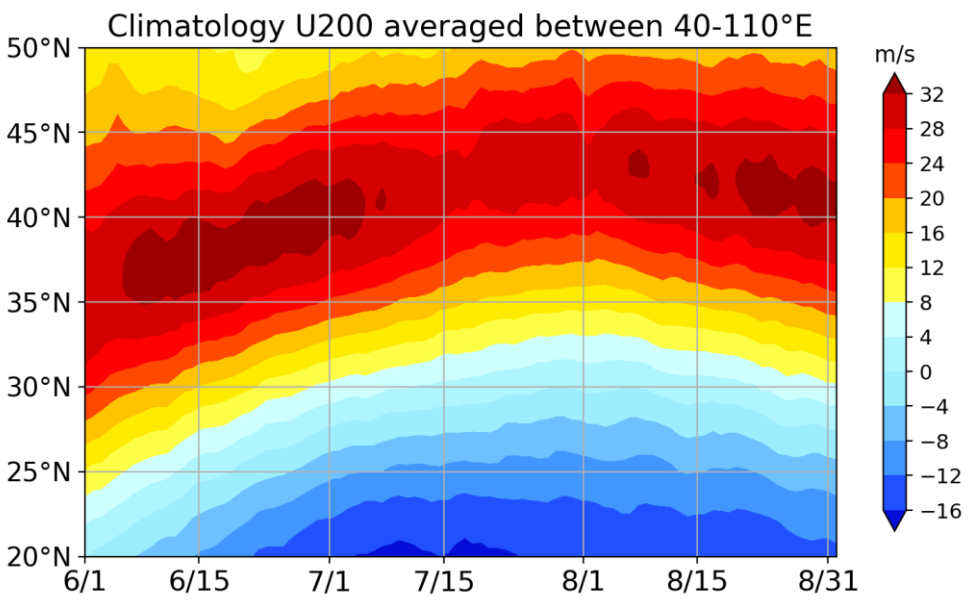

Fig. 4-17. Time-latitude cross section of climatological 200hPa zonal (u) wind (unit: m/s), averaged between 40-110°E from June to August in the latitude range of 20-50°N.

doi:10.6342/NTU202401227

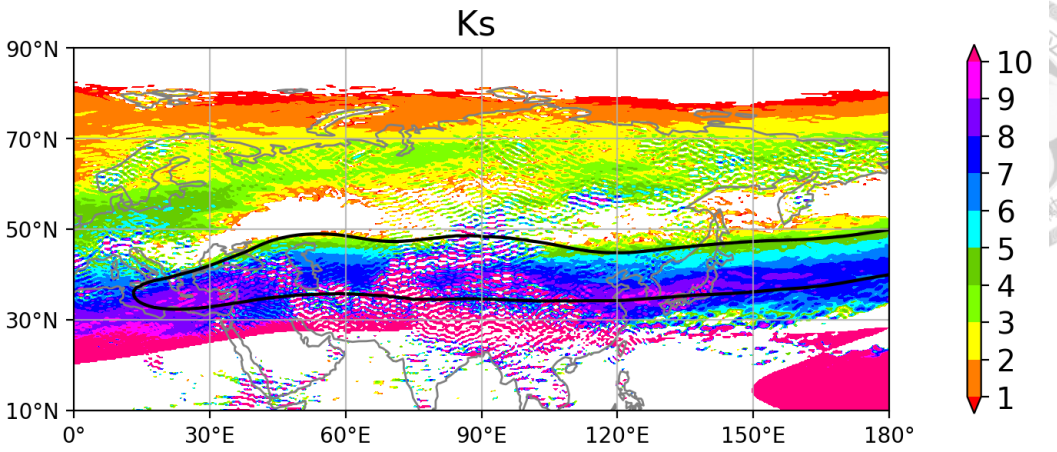

Fig. 4-18. Stationary wavenumber, Ks (shading), calculated from the equation (4). The black line represents the contour of u wind at 200hPa in 20 m/s.

doi:10.6342/NTU202401227

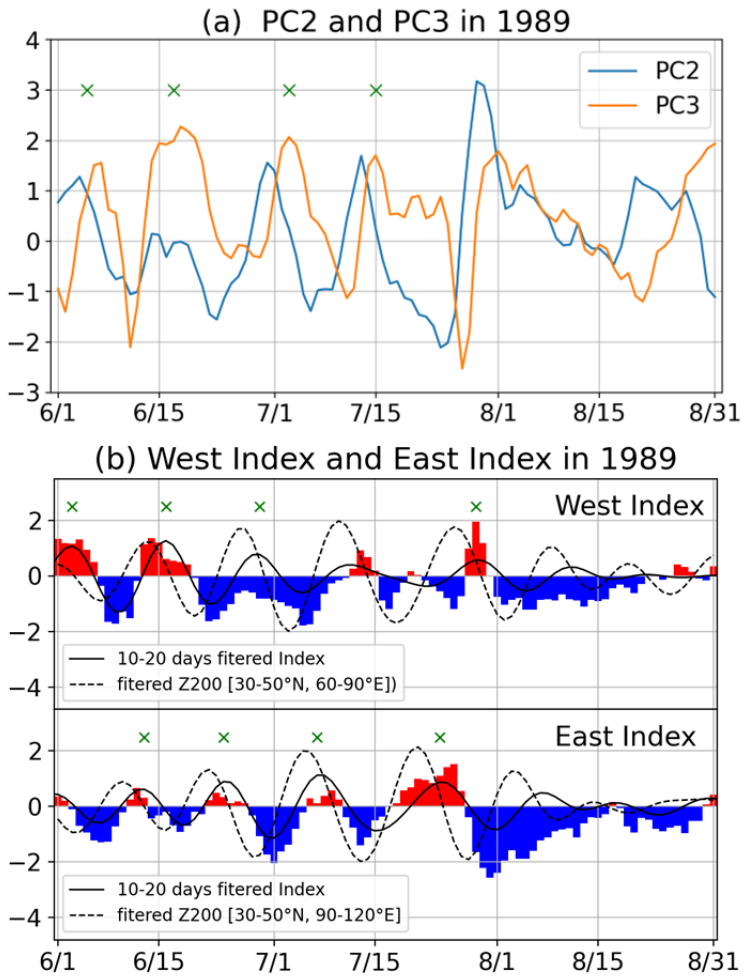

Fig. 4-19. (a) Time series of the PC2 (blue line) and PC3 (orange line) during June to August in 1989. The green dots represent the four positive PC3 peaks. (b) Time series of West Index (25-35°N, 45-65°E) and East Index (30-50°N, 80-100°E). The original Index is shown as red (positive) and blue (negative) bars, and the 10-20 days filtered Index is shown as black solid line. The green dots represent positive peaks of the 10-20 days filtered West Index and East Index with values greater than 0.5. The black dashed lines represent 10-20 days filtered Z200 to the northeast of the West Index (30-50°N, 60-90°E) and East Index (30-50°N, 90-120°E).

doi:10.6342/NTU202401227

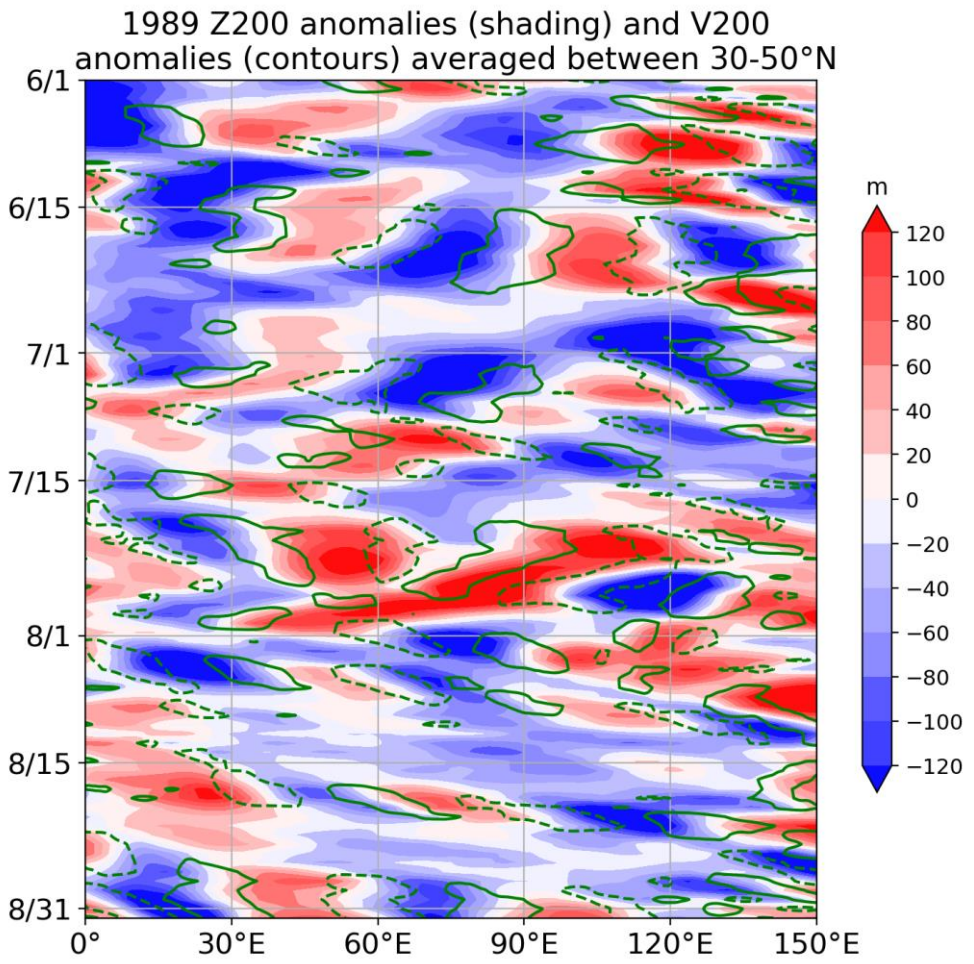

Fig. 4-20. Time-longitude cross section of Z200 anomalies (shading, unit: m) and V200 anomalies (contours, unit: m/s), averaged between 30-50°N from June to August in 1989 in the longitude range of 0-150°E. The green solid (dashed) contours indicate the wind speed of 10 (-10) m/s.

doi:10.6342/NTU202401227

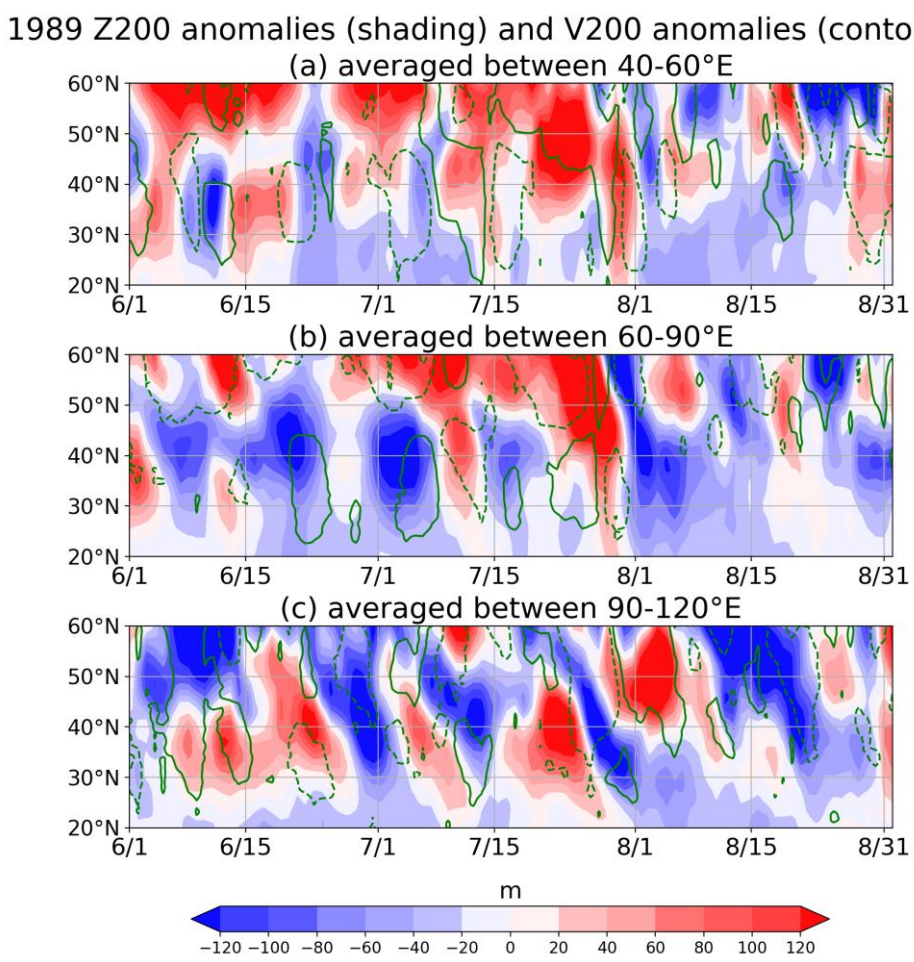

Fig. 4-21. Latitude-time cross section of Z200 anomalies (shading, unit: m) and V200 anomalies (contours, unit: m/s), averaged between (a) 40-60°E, (b) 60-90°E, and (c) 90-120°E from June to August in 1989 in the latitude range of 20-60°N. The green solid (dashed) contours indicate the wind speed of 5 (-5) m/s.

doi:10.6342/NTU202401227

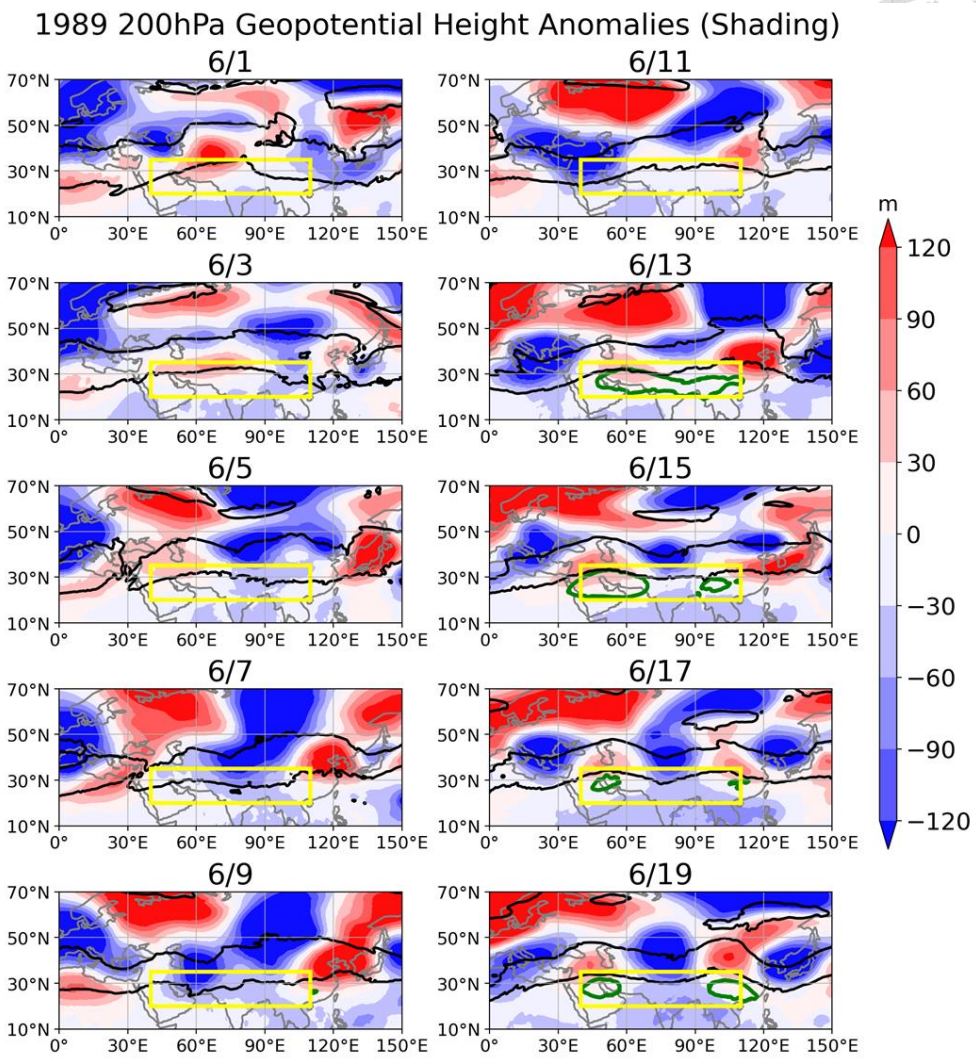

Fig. 4-22. Geopotential height anomalies (shading, unit: m) at 200hPa from 6/1~6/19 in 1989 in every two days. The black line indicates the U200 contour of 20 m/s, and the green line indicates the Z200 contour of 12520 m. The yellow box represents the domain of the EOF analysis (25-35°N, 40-110°E).

doi:10.6342/NTU202401227

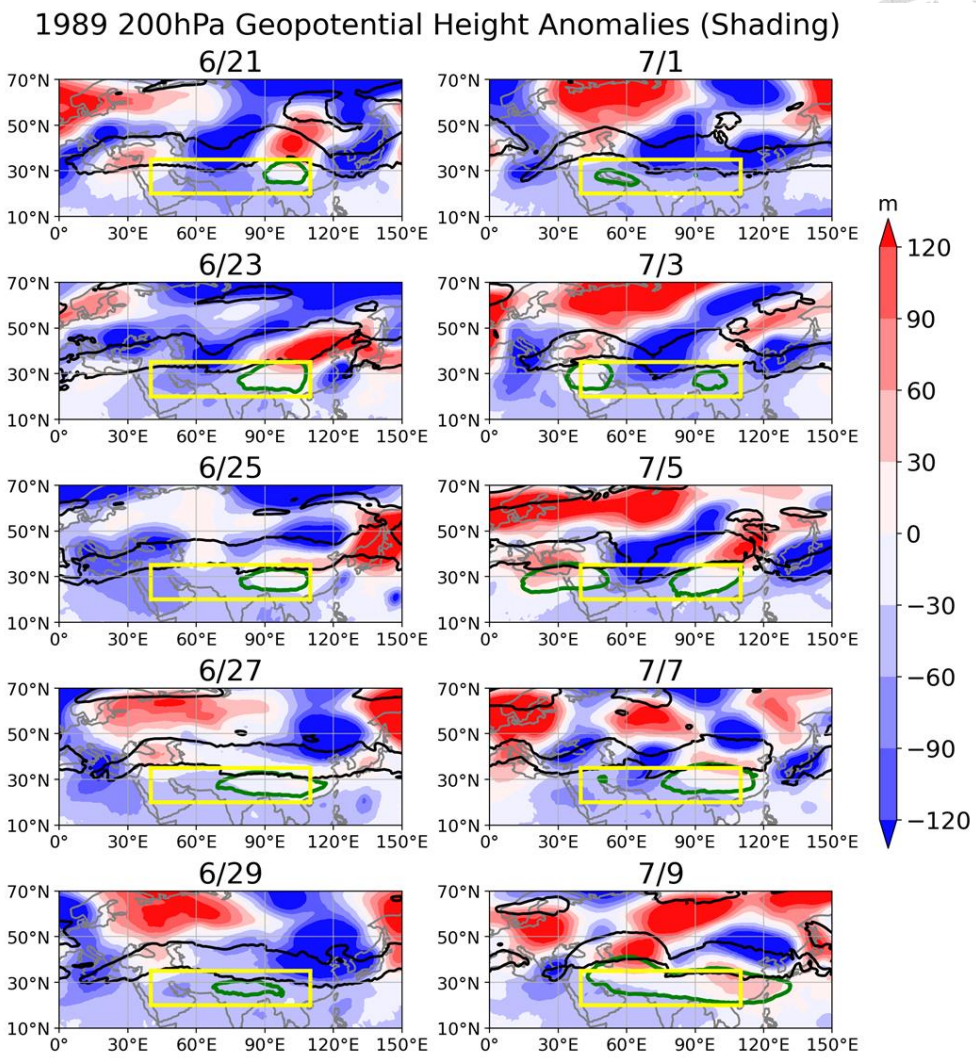

Fig. 4-23. Geopotential height anomalies (shading, unit: m) at 200hPa from 6/21~7/9 in 1989 in every two days. The black line indicates the U200 contour of 20 m/s, and the green line indicates the Z200 contour of 12520 m. The yellow box represents the domain of the EOF analysis (25-35°N, 40-110°E).

doi:10.6342/NTU202401227

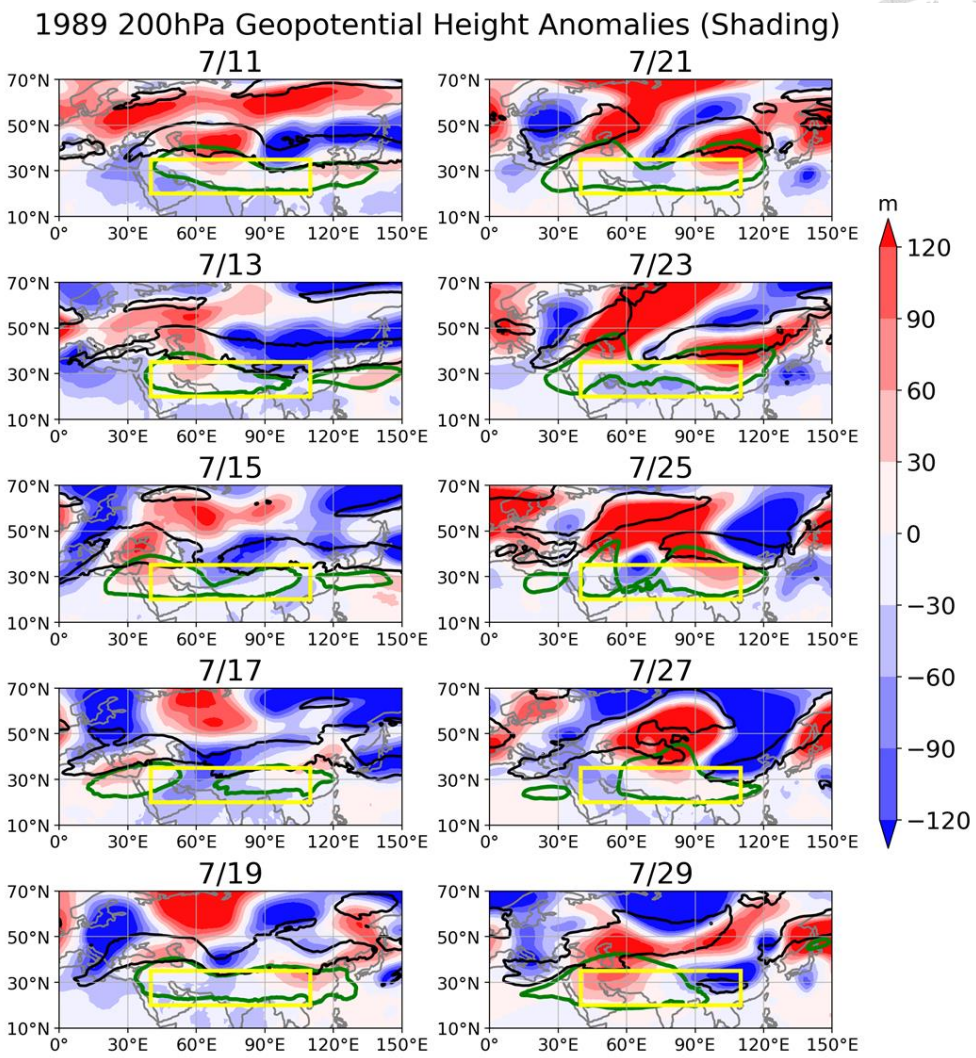

Fig. 4-24. Geopotential height anomalies (shading, unit: m) at 200hPa from 7/11~7/29 in 1989 in every two days. The black line indicates the U200 contour of 20 m/s, and the green line indicates the Z200 contour of 12520 m. The yellow box represents the domain of the EOF analysis (25-35°N, 40-110°E).

doi:10.6342/NTU202401227

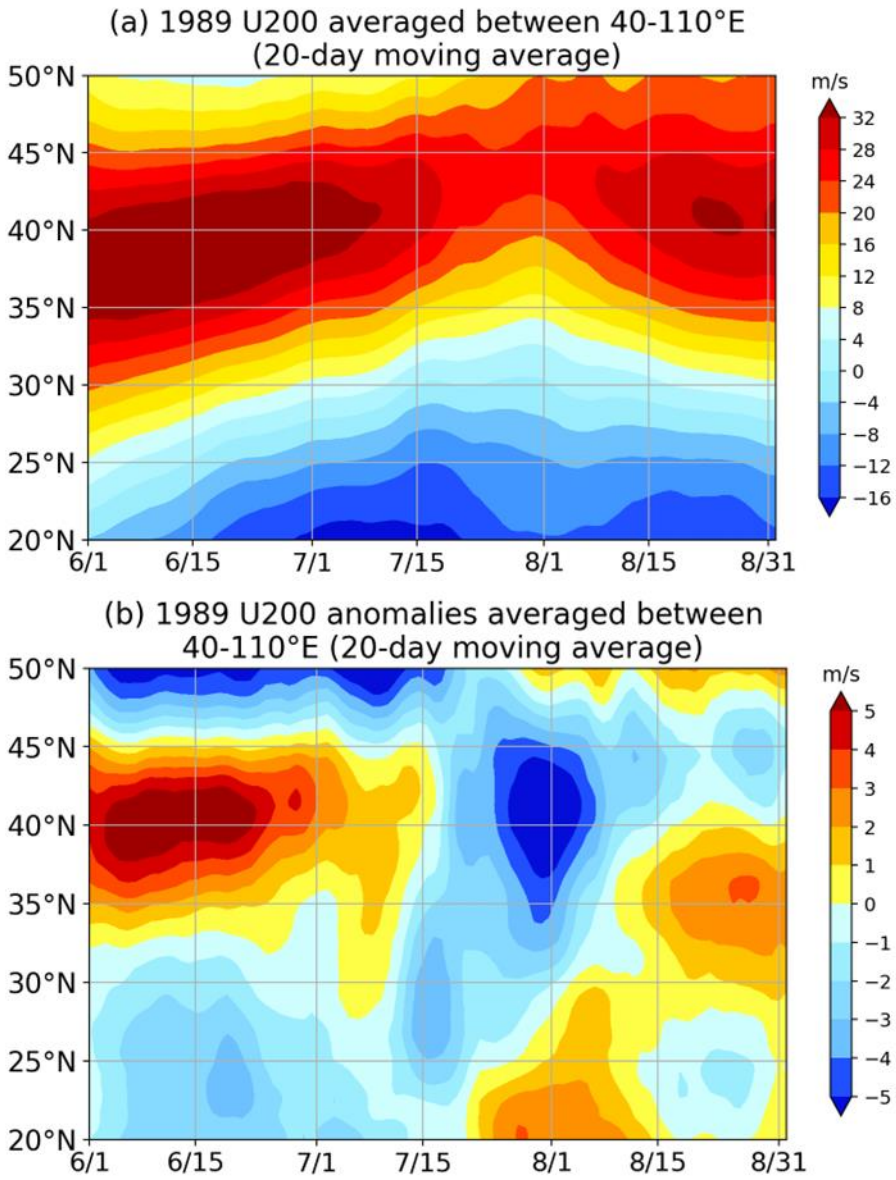

Fig. 4-25. Latitude-time cross section of (a) U200 and (b) its anomalies (shading, unit: m) averaged between 40-110°E, from June to August in 1989 in the latitude range of 20-50°N.

doi:10.6342/NTU202401227

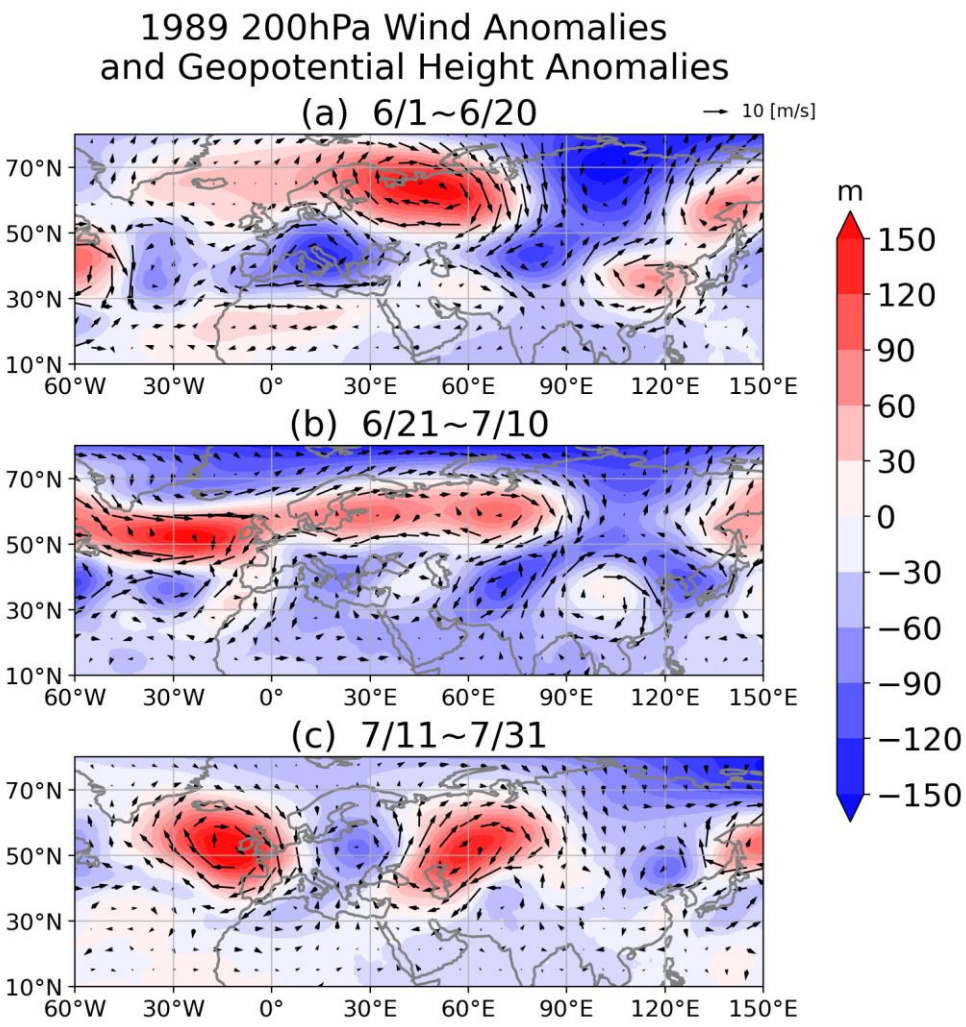

Fig. 4-26. Winds anomalies (vector, unit: m/s) and geopotential height anomalies (shading, unit: m) at 200hPa averaged between (a) 6/1~6/20, (b) 6/21~7/31, and (c) 7/11~7/31 in 1989.

doi:10.6342/NTU202401227

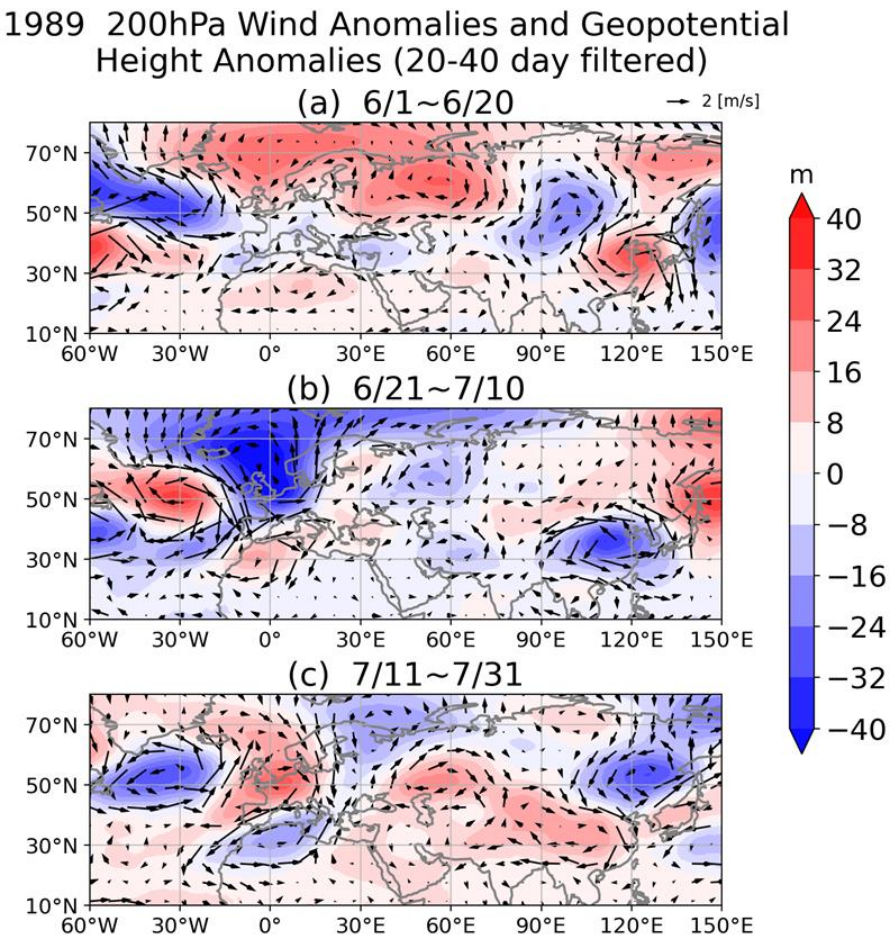

Fig. 4-27. Winds anomalies (vector, unit: m/s) and geopotential height anomalies (shading, unit: m) at 200hPa with 20-40 days filtered averaged over (a) 6/1~6/20, (b) 6/21~7/31, and (c) 7/11~7/31 in 1989.

doi:10.6342/NTU202401227